Impact Induced Landslides as a Mechanism for Diffusive Degradation of Complex Craters found Near the Lunar Southern Pole

By

C. Lauren Talkington

A thesis submitted to the Graduate Faculty of the
Auburn University Department of Geosciences in partial
fulfillment of the requirements for the Degree of Master of
Science

Auburn University
Auburn, Alabama
May 7th, 2022

Approved By:

Chair: Dr. Masatoshi Hirabayashi, Assistant Professor of Aerospace Engineering
and Adjunct Faculty Department of Geosciences
Dr. David T. King, Jr., Professor of Geology
Dr. Stephanie Shepherd, Assistant Professor of Geosciences

Abstract

Throughout its history, the Moon's surface has experienced numerous impact cratering events. Such events have degraded the surface through various processes. Processes include ejecta blanketing, overlapping (cookie cutting), and topographic diffusion. Ejecta blanketing is the process of impact ejecta from other craters covering or partially covering pre-existing craters with their ejecta, degrading crisp topographic features and morphologies. Overlapping, or cookie cutting, is the process in which pre-existing craters have craters from other impactors partially or completely overlap them. Finally, there is topographic diffusion. Topographic diffusion is the dispersal of the lunar regolith through impact events near and overlying pre-existing craters. This study discusses impact driven landslides on crater walls as a key degradation mechanism by considering 16 complex craters around the southern pole of the Moon. By using crater counting, statistical analysis is completed on the crater size populations found on these complex craters' walls, which have varying slope conditions. The results show that the crater populations ranging from 600-800 m diameter are significantly lacking on the walls. It is proposed here that this is likely due to landslide events that cause partial or total erasure of the crater cavities in that size range. Additional analysis of complex crater degradation rate by incorporating the 2014 diffusive model proposed by Fassett and Thomson confirms this interpretation. This diffusive model has been used with success in the study of smaller, simple craters but has not been investigated as a mechanism for degradation of complex craters until now.

Acknowledgements

Completion of this work was supported by the Department of Geosciences at Auburn University, Auburn, Alabama. Part of this research was completed by using data from the PDS Geosciences Node at Washington University at St. Louis and would not have been possible without it. The author thanks research and travel support provided by Auburn University College of Sciences and Mathematics (COSAM), Auburn University Geosciences Advisory Board (GAB), and the Montgomery Gem and Mineral Society. Additionally, the author thanks the support of her committee, Dr. Masatoshi Hirabayashi, Dr. David King, Jr., and Dr. Stephanie Shepherd for their support and guidance in completing this research, none of it would have been possible without your continued dedication to me and all your students. Dr. Hirabayashi, thank you for believing in me and pushing me to reach my goals. I owe my success thus far to your leadership and mentorship. Dr. King, thank you for opening my eyes as an undergraduate to the world of possibilities in studying planetary science. I took your Lunar and Planetary Geology course without expectations, and it has changed my life. Dr. Shepherd, thank you for your advice and support during what arguably was the most challenging period of my life. Thank you to Mr. Pedro Montalvo for taking a chance on me my senior year of undergrad and teaching me the ropes for crater counting. I would not have been able to complete this work without your help. Thank you to my Mother and Father for being patient with me throughout this process, I have learned more from you than you know. Thank you to all colleagues, staff, faculty, friends, and neighborhood baristas and coffee shop friends that have walked alongside me during this process and have cheered me on from near and far. Thank you to my grandmother Meme, for always being a listening ear and offering your advice. Furthermore, to my grandparents that are no longer with me, but always in my heart. Meemaw, Deedee and T, thank you for the advice, letters and wisdom that only in recent years has come to be realized. Starting and completing a project on any level can be a daunting task, but with the right support system, I have learned that I can accomplish anything I put my mind to.

Table of Contents

Abstract……..……..**2**

Acknowledgements……...……...**3**

Table of Contents……...……..**4**

List of Figures……..……**6**

List of Tables……**8**

1. Introduction……..……...…..**9**
2. Crater distributions on complex crater walls…….……...…….**.....16**
    a. Crater counting approach……...…..**16**
        i. Visualization of the Complex Craters……..…**16**
        ii. Crater Data Capture……..…**21**
        iii. Slope Conditions for Crater Data……..…...**24**
    a. Lack of craters greater than 1 km……...…….…..**28**
3. Magnitude of topographic diffusion on complex craters……..…..……..**35**
    a. Formulation of erosion and accumulation depths……..…….**.....35**
    b. Variations in erosion depth with crater size…….……**38**
4. Discussion…….**.....41**
    a. Mixing of ancient water with mass movement materials……**46**
    b. Internal heat and impact mixing contributing to water distribution……**48**
    c. Ages of highly degraded Nectarian and pre-Nectarian craters……..…**52**
    d. Low size-dependence of complex craters' topographic diffusion……..…..**53**
5. Conclusions……..**55**
6. References…….……..…..**56**

7. Appendix……..……**64**

List of Figures

Figure 1. Scott (48.5 E, -82.4N) and Amundsen (83.1E, -84.4N) using ArcMap 10.7.1. Data from: LOLA/LRO PDS Geosciences Node WUSTL. There are two possibilities: Topographic diffusion and ejecta blanketing……..**15**

Figure 2. LDEM_80s_20m.jp2 within ArcMap 10.7.1. Yellow circles denote the 16 craters included within our analysis. The complex crater morphologies are not clear within this data layer……**19**

Figure 3. Definition of the wall boundaries and crater counting processes of Faustini within ArcMap 10.7.1 utilizing Crater Tools [Kneissl et al., 2011]. The blue lines show the defined wall area, and the red circles are the counted craters. The color shows elevation with units of m. This map is centered at (-87.23N, 84.5E)…….…….**23**

Figure 4: The 16 complex craters included within our analysis as viewed using ArcMap 10.7.1. DEM data (PDS Geosciences Node), Slope and Hillshade Overlays, and the CraterTools add in toolkit (Kniessl et al., 2011). The black dashed lines represent the areas considered for our analysis. The blue lines indicate regions counted by Deutsch et al., (2020). The magenta boxes indicate regions counted by Tye et al., (2015)……...**25**
.
Figure 5: Map illustrating the crater counts and rim buffers in the wall region of Faustini (84.8ºE, -87.23ºN) using ArcMap 10.7.1 and CraterTools. At this scale we can see the crater emplacements clearly, illuminated by the Hillshade overlay mimicking the Sun's light at an angle of 30 degrees……**26**

Figure 6: Rim buffer thicknesses of 100 m (blue) and 500 m (green) using Arcmap 10.7.1, CraterTools (Kniessl et al., 2011), and the Buffer (Analysis) Tool…….……..**27**

Figure 7: Histogram plots showing the number of craters found within each size bin. The first histogram used 20 m buffers. The second histogram used 100 m buffers. The third histogram used 500 m buffers. The mode crater size analyzed remained in the > 700 m crater population bin…….……..…**29**

Figure 8: Crater Size Frequency Distribution plots (CSFDs) of craters on the walls of the 16 complex craters around the lunar south pole. The vertical dashed lines give the 600-800 m transition……....**30**

Figure 9: The individual CSFDs of the 16 complex craters found within our analysis. The Red dots with error bars indicate our crater counts for each complex crater. The blue line indicate the Neukum model age based on our counts. The green lines indicate the model age as derived from Deutsch et al., (2020), Tye et al., (2015), and Cannon et al., (2020)…….…**32**

Figure 10: Crater Size Frequency Distribution Plots (CSFDs) of Amundsen (A), Faustini (B), Haworth (C) and Shoemaker (D). The orange CSFDs represent the floor counts. The green PF lines represent the age given by the wall counts. The blue PF lines represent the age given by the floor counts. (Neukum et al., 2001)……...**34**

Figure 11: Schematic of computing the number of erased craters on a crater wall. The black line is the Neukum model, the green line is the visible crater number on the floor, and the red line is the visible crater number on the wall…….**37**

Figure 12: Resurfacing of the 16 complex craters near the lunar southern pole. Panel a shows the resurfacing depth as a function of age. The color map describes the crater diameter variation. The dashed line is a scaling relationship. Panel b gives the size independence of the κt value as a function of the crater diameter. The solid line shows the scaling relationship for small, simple craters less than 5 km in diameter (Fassett and Thomson, 2014). The color map is the Neukum-based model age. Panel c shows the variations in the κt value with age. Panel d illustrates the κt value corrected by the size dependency given in Panel b. The color maps of Panels c and d represent the crater diameter. For Panels c and d, the results by Fassett and Thomson (2014); Fassett et al., (2018) are only applicable to the ages shorter than 3.8 Gyr……**40**

Figure 13: Presence of ancient water affected by topographic diffusion driven accumulation, impact mixing, and internal heat. For all of the panels, the red lines are the depth affected by impacts mixing, while the blue lines are the depth driven by topographic diffusion driven accumulation on a crater floor. The black lines describe the thermal threshold. The cyan regions are areas where ancient water may be preserved. Panels a, b, and c show cases when the surface temperatures are 50 K, 75 K, and 100 K, respectively…….…….**50**

List of Tables

Table 1: 16 crater counts on the walls of complex craters along with their wall area. The selected target complex craters were also analyzed by Tye et al., (2015), Deutsch et al., (2020), and Cannon et al., (2020)……..**17**

Table A1. Data Compiled from this study……..…..**63**

1. Introduction

Lunar surfaces over the Moon's history have constantly been bombarded, which causes their topographic conditions to change. Impact craters are the most common landforms on the lunar surface, with morphologies ranging from fresh to highly degraded (Öpik 1960; Ross 1968; Melosh 2011). When a crater is newly emplaced or considered 'fresh', it possesses crisp morphologies (i.e., clear rims, sloping walls, central uplift in complex craters). However, as the crater remains exposed to constant impact bombardment processes, it is gradually degraded. There are three major degradation processes: overlapping (Minton et al., 2015; Hirabayashi et al., 2017), ejecta blanketing (Bandfield et al., 2017), and topographic diffusion (Fassett and Thomson 2014; Fassett 2016; Hirabayashi et al., 2017; Minton et al., 2019). Crater overlapping, also known as cookie-cutting, (Minton et al., 2015; Riedel et al., 2020; Woronow 1977) is a process in which a newly emplaced crater overlays existing craters and immediately erases them. Ejecta blanketing is a process that buries existing craters by ejecta from a new crater (e.g., Orientale basin ejecta; Fassett et al., 2011). Topographic diffusion is a process that gradually degrades topographic features over a longer timescale. All these degradation processes correlate with each other, likely this gives the process of crater degradation as a whole a dependence on the crater diameter.

Unlike crater overlapping and ejecta blanketing, topographic diffusion occurs by many different physical processes. The original concept of topographic diffusion as proposed by Soderblom (1970) was a degradation process in which a small crater emplacement on a sloping wall of a larger crater may cause asymmetric ejecta blankets due to material moving in the downslope direction, gradually erasing topographic features. As discussed in Riedel et al. (2020), when fresh craters form on slopes, their proximal ejecta deposits move in the downslope

direction (Ross, 1968; Soderblom, 1970). This process, known as sandblasting, allows small craters to degrade the slopes of larger ones by slowly filling them and eventually erasing them completely (Fassett et al., 2011).

Soderblom's model (1970) mathematically described this phenomenon by using a diffusion equation that quantifies topographic evolution driven by mass flows proportional to gravity slopes (Soderblom 1970). Therefore, the equation itself can account for gradual topographic degradation by landslides (Kokelaar et a., 2017). Earlier work also used the diffusion equation to quantify how topographic diffusion affects degradation processes of existing craters and characterize their impact cratering history (Fassett and Thomson, 2014; Fassett et al., 2017; Basilevsky et al., 2018; Ridel et al., 2020). Interestingly, this model is used to model hillslopes here on Earth as well.

The major topographic diffusion processes have been well-argued mainly for smaller, simple craters (Craddock and Howard, 2000; Fassett and Thomson, 2014; Fassett et al., 2017; Hartmann and Gaskell, 1997; Riedel et al., 2020). Topographic diffusion has gradually degraded the craters' bowl-shaped morphologies (e.g., ~200-300 m diameter craters would completely be erased within 3 Gyr on the Moon (Fassett and Thomson, 2014)). Importantly, the degradation rate may change depending on the crater sizes and the impact history. The diffusivity, κ (kappa), increases with age. The larger the crater size, the longer the topographic diffusion time scale becomes. Interestingly, the diffusion coefficient representing the factor of diffusion, κ tends to be high recently (< 1 Ga) and during the early history of the Moon (> 3 Ga). This recent high κ value may give two implications: a recent higher impact flux (Fassett and Thomson 2014) or a higher degradation process of fresh, young craters (Fassett and Thomson, 2014).

Not only do primary cratering events, i.e., meteoroid impacts, contribute to topographic diffusion, secondary cratering events as a result from these initial impacts cause further degradation of the lunar surface (McEwen and Bierhaus, 2006). Secondary craters are able to be determined from simple craters by their morphologies and spatial relationship to one another. These craters are typically found in clusters or chains, or spatially very close to one another. Furthermore, topographic diffusion driven by secondary cratering events may roughly be categorized into two regimes: proximal and distal diffusion (Minton et al., 2019). Proximal diffusion may mainly be driven by additional effects of ejecta blanketing on diffusion and seismic shaking by a crater emplacement. In fact, seismic shaking likely changes the morphology at crater radii from an impact site (Kreslavsky and Head 2012), and additionally from various distances depending on impactor size. Distal diffusion could affect in wider areas from a primary crater as is observed as asymmetric morphological features of craters possibly due to ejecta from Tycho (Bandfield et al., 2017). Basilevsky et al. (2018) studied Copernicus' and Tycho's secondary crater populations. They found that of the 15 ~350-950 m and 8 ~250-650 m diameter craters analyzed, the smaller craters are affected by topographic diffusion at a higher rate than the larger ones, deducing a timescale for this degradation to be proportional to the square of the crater diameter. These secondary crater emplacements cause topographic degradation at various distances from the initial crater and its rim by proximal ejecta blanketing and sandblasting (Speyerer et al., 2016). Given these processes, proximal and distal diffusion may act differently, giving craters unique morphological evolution processes.

On the other hand, topographic diffusion processes of large, complex craters are not well explored or understood. The major reason may result from a diffusion time scale possibly longer than the lunar bombardment history, which may challenge quantitative assessments by looking at

morphological variations in these craters. Complex craters on the Moon (> 20 km diameter) may be diffused on a much longer timescale than small, bowl-shaped craters, implying that the major erasure process is likely cookie-cutting (Riedel et al., 2020).

However, some craters around the lunar south pole exhibit highly degraded morphologies. Figure 1 shows two complex craters at the lunar south pole, Scott (48.5 E, -82.4 N) and Amundsen (83.1 E, -84.4 N). Both complex craters are ~100 km in diameter. Scott (48.5 E, -82.4 N) is highly degraded (3.8 + 0.1, -0.1 Ga [Deutsch et al., 2020]), and does not exhibit clear crater morphologies such as the crater rims and crater floor. On the other hand, Amundsen (83.1 E, -84.4 N) is relatively fresh, exhibiting clear rim morphologies. Amundsen also has its central peak from the initial uplift from the impactor. Interestingly enough, Amundsen's model age is 3.9 + 0.1, -.1 Ga. This study considers that the highly degraded state of Scott resulted from topographic diffusion as ejecta blanketing could have only given a limited influence on degradation. Amundsen's observed depth is ~ 7.0738 km while Scott's is ~ 6.3044 km. We see a clear trend that Amundsen is deep, i.e., fresh, while Scott is shallow. On the other hand, using a scaling relationship of the depth/Diameter (d/D) ratio for complex craters, $d/D = 1.044D^{0.301}$ (Pike, 1974), we obtain Amundsen's depth as 4.2 km and Scott's as 4.3 km, which are consistent with 100 km diameter fresh complex craters on the Moon (~5 km deep) (Pike 1980b; Robbins et al., 2017). For Scott, the difference between the observed depth and the predicted initial depth, i.e., -2.87 km, indicates an accumulated layer of regolith that degraded this crater. However, Cannon et al. (2020) showed that the maximum ejecta deposits at the south pole would only be up to 1 km. Layers within this gap may be filled by topographic diffusion.

This study proposes that topographic diffusion in complex craters results from enhanced landslides driven by impacts forming or capable of forming crater emplacements on their walls.

We determine they are enhanced, because they are impact driven, and as a result of larger impactors hitting the surface. As shown in the upcoming sections, we observe that there are fewer craters on the walls than on the crater floors. Considering the same impact flux in these two regions (and thus the same age), we infer that the crater population gap between these two areas implies different degradation speeds. Thus, the walls have higher crater degradation rates because craters there can be erased along a shorter timescale. Impact cratering creates surface topography and differences in the surface, weakening portions of the walls (Xiao 2020). This promotes mass movement events over large areas and time scales. Brunetti et al. (2015) compared landslides in impact craters on the Moon in contrast to Mercury and found that Mercury's rockslides are found within smaller craters. Their investigations deduce this is likely due to gravity differences. This research implies that the Moon has a higher degradation rate (Brunetti et al., 2015). Our research does not investigate exterior landslide features, however, in a previous study, (Boyce et al., 2020) LROC images were analyzed, and they found evidence for landslides in regions free from ejecta blanketing near Tsiolkovsky, indicating their role in degradational processes, namely, topographic diffusion.

Here, analyzing the walls of 16 complex craters located in the south polar region (Deutsch et al., 2020), we show that on complex crater walls, craters larger than 600 m - 800 m diameter are likely depleted. We infer this finding as the mechanism that topographic diffusion is accelerated by a series of enhanced landslides that were caused by impactors capable of forming crater emplacements larger than 600 m - 800 m diameter. Thus, topographic diffusion may be more enhanced than the process driven by sandblasting initially proposed by Soderblom, particularly when craters are fresh and possess highly sloping walls. To explore this issue, we use the following techniques. First, I use a crater counting approach to statistically analyze the

crater distribution on the walls of these complex craters. Second, calculate the erosion depth for the complex craters. Third, compare the findings on the walls to some of the floor regions. Fourth, give the production functions for the complex craters. Fourth, quantify how topographic diffusion affects complex crater degradation by calculating their eroded depths and calculate their resurfacing depth of the complex craters as a function of age. Finally, this manuscript will offer some insight into potential conditions that may alter complex crater degradation.

The present study is to discuss approaches and results for each technique in one section, instead of arguing them separately. Section 2 focuses on the crater counting analysis and methods. Section 3 discusses the magnitude of topographic diffusion on complex craters. Section 4 offers a discussion of results. Section 5 outlines our conclusions. Section 6 offers discussions of our results. Finally, the Appendix offers our data table used within our analysis and supplemental information. This work is complementary to recent work analyzing the crater wall of an unnamed ~3.4 km simple crater in the Schrödinger basin to show dry granular flows, but unique because we address the surface and impact conditions in complex craters (Kumar et al., 2013).

Scott

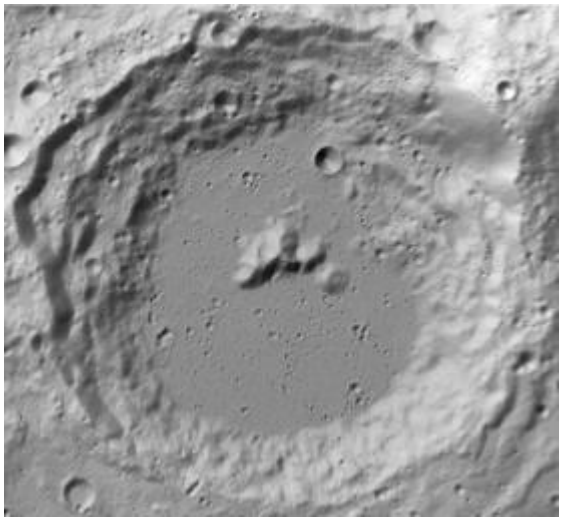

Amundsen

Figure 1: Scott (48.5 E, -82.4N) and Amundsen (83.1E, -84.4N) using ArcMap 10.7.1. Data from: LOLA/LRO PDS Geosciences Node WUSTL. There are two possibilities: Topographic diffusion and ejecta blanketing.

Objective

In this research, I analyze 16 complex crater morphologies found near the lunar southern pole that are partially or completely affected by Permanently Shadowed regions (PSRs). The 16 complex craters have varying ages (4.18-3.15 Gyr), diameters (107.8-20.9 km), morphologies (presence or lack of central uplift, terraces, and clear wall and floor boundaries), and degradation states. By assessing these characteristics, the aim is to characterize the rate at which lunar complex craters are eroded by topographic diffusion.

2. Crater distributions on complex crater walls

2.1 Crater Counting Approach

2.1.1 Visualization of the Complex Craters

To complete our crater counting analysis, we used ArcMap 10.7.1 and the CraterTools add-in toolkit to count smaller craters on the walls of complex craters found within the southern pole of the Moon (Kniessl et al., 2011). We selected 16 complex craters chosen from prior research (Deutsch et al., 2020; Tye et al., 2015; Cannon et al., 2020) to use the available geologic information such as the sizes, morphologies, slope conditions, and degradation states for comparison (Figure 2). The chosen complex craters are provided in Table 1. They range in sizes 20.9-107.8 km in diameter. The different morphologies vary from presence or lack of terraces, central peaks, evidence for partial or total landslide coverage and defined flat floor regions. Their absolute and estimated model ages range from 4.18+0.02, -0.02 Ga to 3.14+0.05, -0.08 Ga (Deutsch et al., 2020; Tye et al., 2015; Cannon et al., 2020). These different ages, sizes, crater counts, and wall areas can be seen in Table 1.

Table 1. 16 Crater counts on the walls of complex craters along with their wall area. The selected target complex craters were also analyzed by Tye et al., (2015), Deutsch et al. (2020), and Cannon et al., (2020).

Complex Crater	Diameter (km)	Crater Counts	Wall Area (km^2)	Absolute, Estimated [**], [***] and Re-Calculated model age s (Tye et al., 2015**, Cannon et al., 2020***)	Resurfacing Depth (km)
Haworth	51.4	710	1858.32	4.18 + 0.02, -0.02 [**]	1.198350577
Shoemaker	51.8	229	1747.36	4.15 + 0.02, -0.02 [**]	1.41596146
Faustini	42.5	388	1049.87	4.10 + 0.03, -0.03 [**]	0.7736585927
Unnamed 1	57.7	1012	1760.1	3.9 + 0.1, -1	0.4066828781
Cabeus B	59.6	622	1912.46	3.9 + 0.1, -.1	0.8882718421
de Gerlache	32.7	202	510.68	3.9 + 0.1, -.1	1.270643828
Nobile	79.3	648	3619.11	3.8 + 0.1, -0.1	1.248322068
Slater	25.1	238	326.527	3.8 + 0.1, -0.1	0.1179587458
Scott	107.8	1213	6282.7	3.8 + 0.1, -.1	1.115641215
Sverdrup	32.8	172	583.98	3.8 + 0.1, -.1	0.3889602852
Unnamed 2	26.8	104	479.65	3.7 + 0.1, -.1	1.297781502
Cabeus	100.6	1001	7763.9	3.88 [***]	1.6601794
Unnamed 3	22.3	129	341.255	3.4 + 0.1, -.5	0.02960806899
Weichert J	34.9	118	830.05	3.2 + 0.3, -.1	0.04234845691
Shackleton	20.9	14	310.797	3.51	0.01553132272
Amundsen	103.4	1393	5876	3.9+0.1, -.1	0.3564414216

To visualize the topographic information using ArcMap 10.7.1, I used the digital elevation model (DEM) (ldem_80s_20m.jp2) data collected by the Lunar Orbiter Laser Altimeter (LOLA) on board the Lunar Reconnaissance Orbiter (LRO) available through the PDS Geosciences Node at Washington University of St. Louis (Riris et al., 2008) (https://pds-geosciences.wustl.edu/lro/lro-l-lola-3-rdr-v1/lrolol_1xxx/data/lola_gdr/polar/jp2/). The DEM has a resolution of 20 m/pixel, height uncertainty of less than ~10 cm, and accuracy of ~1 m (Riris et al., 2008; Barker et al., 2016; Barker et al., 2021). The use of the DEM was preferred over the use of LRO NAC images due to the permanently shadowed regions (PSRs) within these craters. The nature of the PSR's prohibited me from seeing the surface of some or in some cases all of the interior morphologies of the crater by imagery alone. By using elevation data, I generated false images of the regions to identify crater-like morphologies easily (Figure 3). This allowed me to count crater diameters ranging from sub km diameters to 35 km on the walls. This study defined craters as circular features with centralized depressions and included these features within the analysis. There are likely to be some small craters (< 99 m in diameter) that were unintentionally omitted from the analysis due to the resolution limit, potentially adding bias to this study by deflating smaller crater populations. However, the influence of this issue is minimal when observing the geologic trends targeted in this study, i.e., the depletion of craters smaller than 600-800 m diameter, and how this is tied to quantifying topographic diffusion. Additionally, I chose to only consider primary craters within this analysis. The inclusion of only primary craters eliminates craters formed by ejecta or boulders from initial impacts. This constraint permitted me to omit craters found in clusters and chains, as these are the most likely characteristics of secondary craters.

Initially, it was challenging to use only DEM data to distinguish terraces or crater emplacements on the walls of complex craters, shown in Figure 2. I used the coordinate data presented in Deutsch et al., (2020) to find the complex crater locations within the DEM and individually create false images by using slope and hillshade maps. I utilized the Clip tool to cut the DEM down to analyze each complex crater individually (Figure 3). By doing this, this assured that ArcMap 10.7.1 would run smoothly with future layers added to the DEM to further analyze the crater. Working with one complex crater at a time, allowed ArcMap 10.7.1 to operate more efficiently.

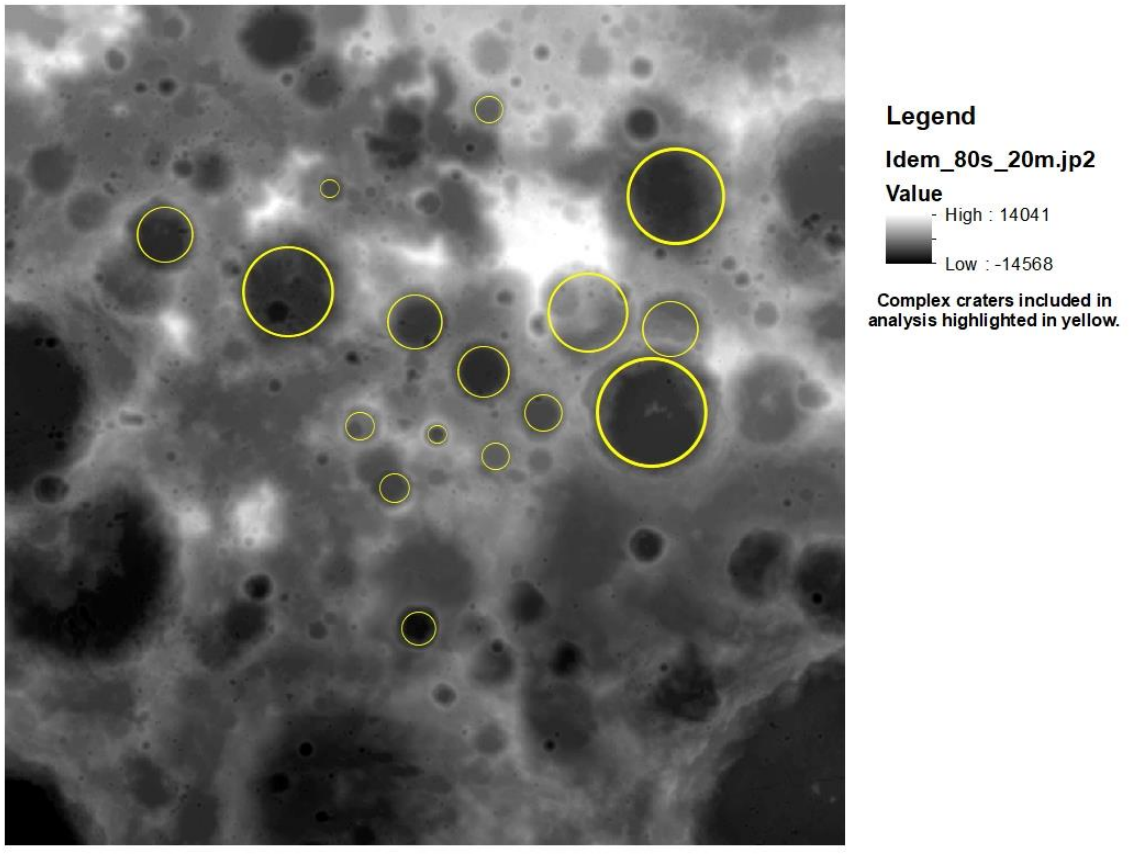

Figure 2: LDEM_80s_20m.jp2 within ArcMap 10.7.1. Yellow circles denote the 16 craters included within our analysis. The complex crater morphologies are not clear within this data layer (PDS Geosciences Node, WUSTL).

The only viewable features using only DEM layers are the exterior complex crater rims, surrounding regolith, and some central peaks. To remedy this, I incorporated the addition of a slope layer by using the Slope (Spatial Analyst) tool to create a slope gradient over the complex crater walls. This helped me visualize the variations in slope in high definition (20 m/pixel) (Riris et al., 2010). The slope symbology was set to be classified by natural breaks (jenks), defining the slope categories for each color to be separated into 9 different slope ranges. This interval increased each slope category by ~ 7º to 11º depending on the complex crater. The algorithm used for defining slope, S, is given as Equation (1).

$$S = arctan(\sqrt{([dz/dx]^2 + [dz/dy]^2)}) * \frac{180}{\pi} \quad (1)$$

where z is the vertical direction, and x and y represent the horizontal directions. The change rate of the surface elevation in the x direction is given as dz/dx and the y direction dz/dy (Borrough and McDonnell, 1998; Eberly 1999; Ligas and Banasik, 2011; Hofmann-Wellenhof et al., 2011). The first slope classification was defined to be < 10°, this would define the region considered to be the flat floor regions and eventually would be excluded from the counting area (Deutsch et al., 2020; Tye et al., 2015; Cannon et al., 2020).

The next layer added to view the complex crater morphology was the Hillshade layer. This layer used the Hillshade tool to create a grayscale 3D representation of the terrain surface, allowing the Sun's relative position to be considered (Burrough and McDonnell, 1998). In this research, I used an altitude angle of 30º and azimuth angle 315º with a contrast of 3 to view the surface. Next, I overlaid the hillshade layer on top of the slope layer and set the transparency to 35% to enhance the slope overlay underneath. The combined use of slope and hillshade overlays

granted visibility of the complex craters regardless of their proximity or affect from the permanently shadowed regions.

2.1.2 Crater Data Capture

With the visualization complete, next began the crater counting process on the walls of the complex craters by using the CraterTools add in toolkit [Kneissl et al., 2011]. Figure 3 shows an example of the crater counting process done in this analysis and can be referred for the following discussions. First, I navigated to the CraterTools toolbar and created two shapefiles, defining the crater counting layer and wall area layer. Once this has been completed, the next task is to define the area to be considered by creating two polygons around the outer and inner rims of the complex crater. The first polygon defines the outer rim of the complex crater from the surrounding exterior of the complex crater. These boundaries were defined by the variations in slope between the rim of the complex crater and the contrasting flat surrounding surface. Some issues with this arose in complex craters that are emplaced near other complex craters, where the rim was determined by the border between the two complex craters. The second polygon defines the boundary between the wall and the flat floor region. Like the outer rim, the defined polygon was derived by slope variations between the sloping wall and the interior flat floor region. The area that was considered for this boundary was the point at which the walls no longer sloped bordering the flat floors. I cited previous research (Deutsch et al., 2020) in determining this interior boundary (< 10°). Depending on the degradation state, this becomes more difficult to define as some complex craters in this analysis are highly degraded and show signs of landslide material partially or totally covering their floors. Furthermore, this transition can be complicated due to the number of crater emplacements on the walls, allowing for a greater amount of

topographic diffusion to blend the wall and floor regions, and finally landslide material that has accumulated at the floor. Landslide morphologies on the walls are characterized by flat terraces shown in sequence to one another, however, on the floor landslide material can be characterized by shallower gradients in slope, ribbony geologic features, and oftentimes appear analogous to alluvial fans here on Earth. The boundary for these craters was determined based on best judgement to what material was considered to be landslide material and utilizing the slope layer to distinguish variations in slope from sloping (yellow) to flat (blue) by following morphologies previously outlined. I calculated the area in km^2 by calculating the geometry within the area attribute table. To calculate the true area of the counted region, I simply subtracted the inner area polygon (floor) from the outer area polygon (walls), shown in Table 2.

Within the Create Features tab, I highlighted 'Standard' under the crater counting layer and chose the 3-point counting method within the CraterTools tool kit (Kneissl et al., 2011). I found this method is more accurate than the 2-point crater counting method, because it utilizes three points around the target crater and extrapolates the rim through those points. This process was replicated until all the craters on the walls of the complex craters were counted.

Craters on the walls were defined as clear circular features with central depressions. Careful attention was taken to generate the most accurate crater populations as possible by following these criteria. The pre-determined slope conditions of the walls made it imperative for the crater counting process to be as precise as possible. This differs from counting craters on the floors because the floors do not experience sloping conditions in complex craters. Additionally, on the walls crater emplacements can exhibit ellipsoidal morphologies due to the walls slope. This ultimately can cause the observed diameters to be greater than what is actually emplaced, however, it is noted that this trend is predominantly found in small to midsize emplacements.

This analysis spanned crater sizes from ~100 m - 35 km in diameter (Appendix). The lower limit for considering features as craters is determined by the resolution of the DEM. Features that were smaller but did not have a central depression (likely boulders) were excluded from the analysis. Craters within the higher slope regions on the walls were considered by the presence of flat regions. This is due to the slope conditions on the walls blending with the sloping of one side of the crater emplacement.

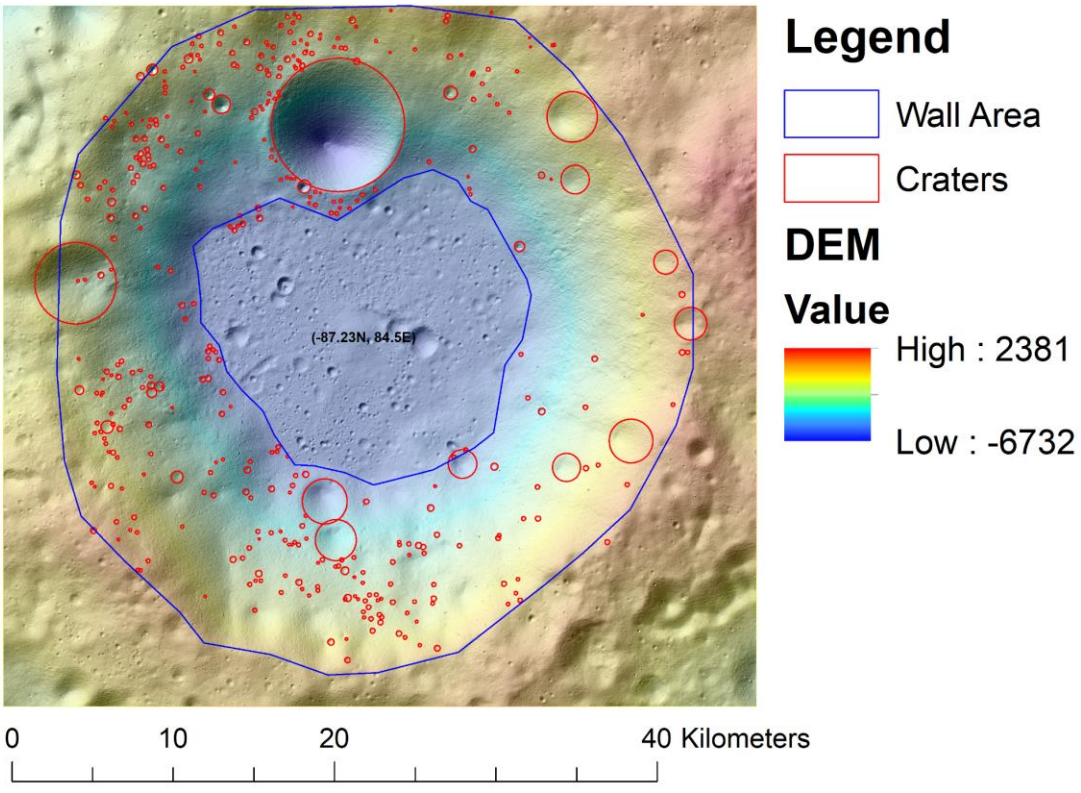

Figure 3: Definition of the wall boundaries and crater counting processes of Faustini within ArcMap 10.7.1 utilizing Crater Tools (Kneissl et al., 2011). The blue lines show the defined wall area, and the red circles are the counted craters. The color shows elevation with units of m. This map is centered at (-87.23N, 84.5E).

2.1.3 Slope Conditions for Crater Data

With the crater emplacement data processed, the next step was to determine the slope conditions for each crater emplacement on the wall (slope measurements found within the Appendix). The importance of this was to see if there were any correlations between crater diameter populations and slope environment of the walls surrounding the emplacement. To do this, I utilized the Buffer (Analysis) Tool and Add Surface Information (3D Analyst) Tool. A 20 m, 100 m and 500 m buffer were created around each crater emplacement. 20 m is determined by the resolution of the DEM as 20 m/pixel (Riris et al. 2008). The completed 16 complex crater illustration can be seen below in Figure 4. The morphologies of the craters range from fresh, exhibiting crisp morphologies, to highly degraded. This transition can be seen in investigating the complex craters. Initially, looking at Amundsen (A), this complex crater illustrates what a clear crater would look like. It has clear boundaries between the floor and wall regions, exhibits a central peak or uplift, and its walls show signs for landslide events i.e., terraces. On the other hand, looking at Scott (H), this crater is highly degraded as these features are not as well defined. Landslide material either completely or partially covers the craters morphologies and can be seen within Cabeus B (C), Shackleton (I), Unnamed 1 (M), and Weichert J (O).

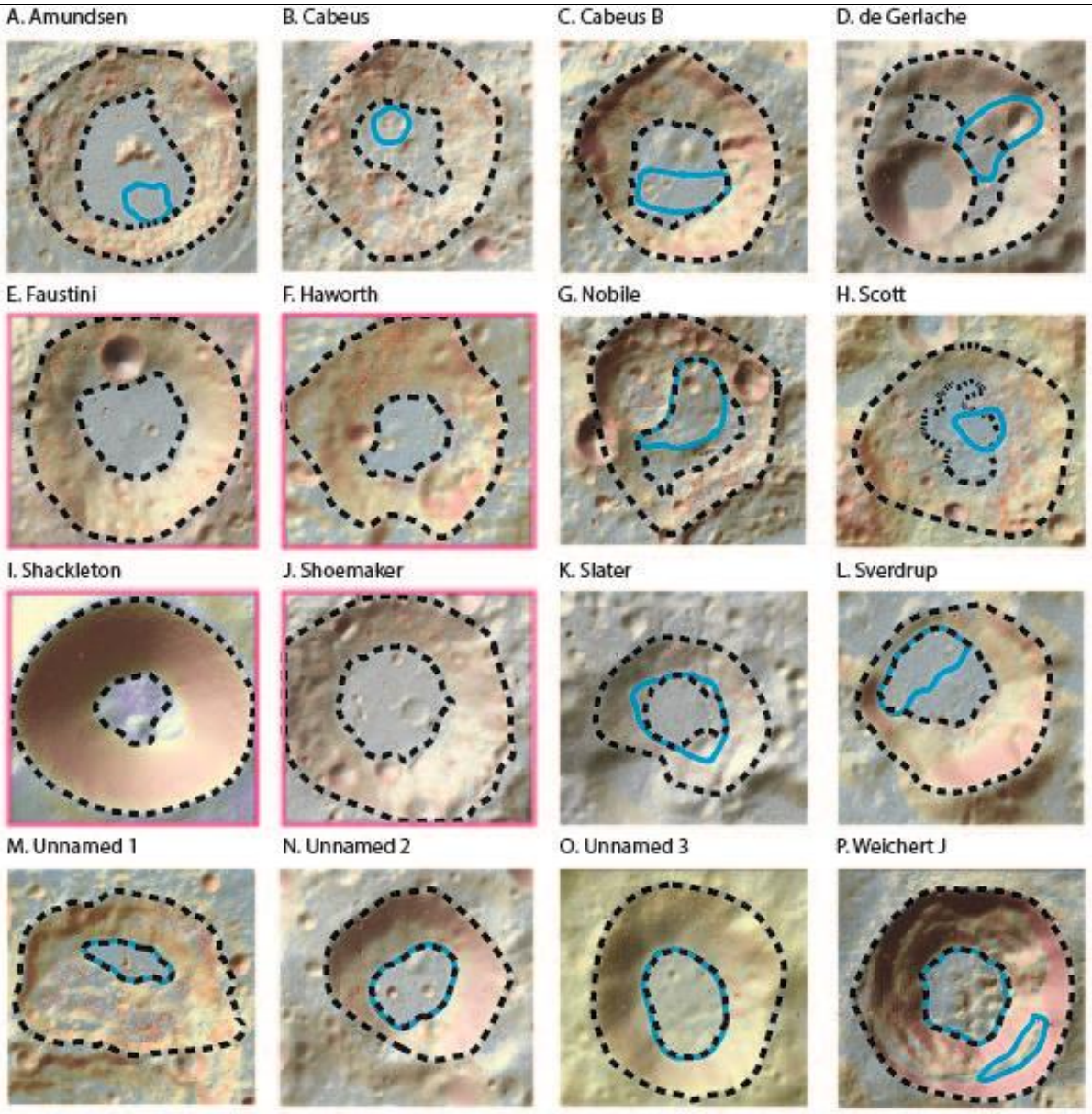

Figure 4: The 16 complex craters included within this analysis as viewed using ArcMap 10.7.1, DEM data (PDS Geosciences Node), Slope and Hillshade Overlays, and the CraterTools add in toolkit (Kneissl et al., 2011). The black dashed lines represent the areas considered for our analysis. The blue lines indicate regions counted by Deutsch et al., (2020). The magenta boxes indicate regions counted by Tye et al., (2015).

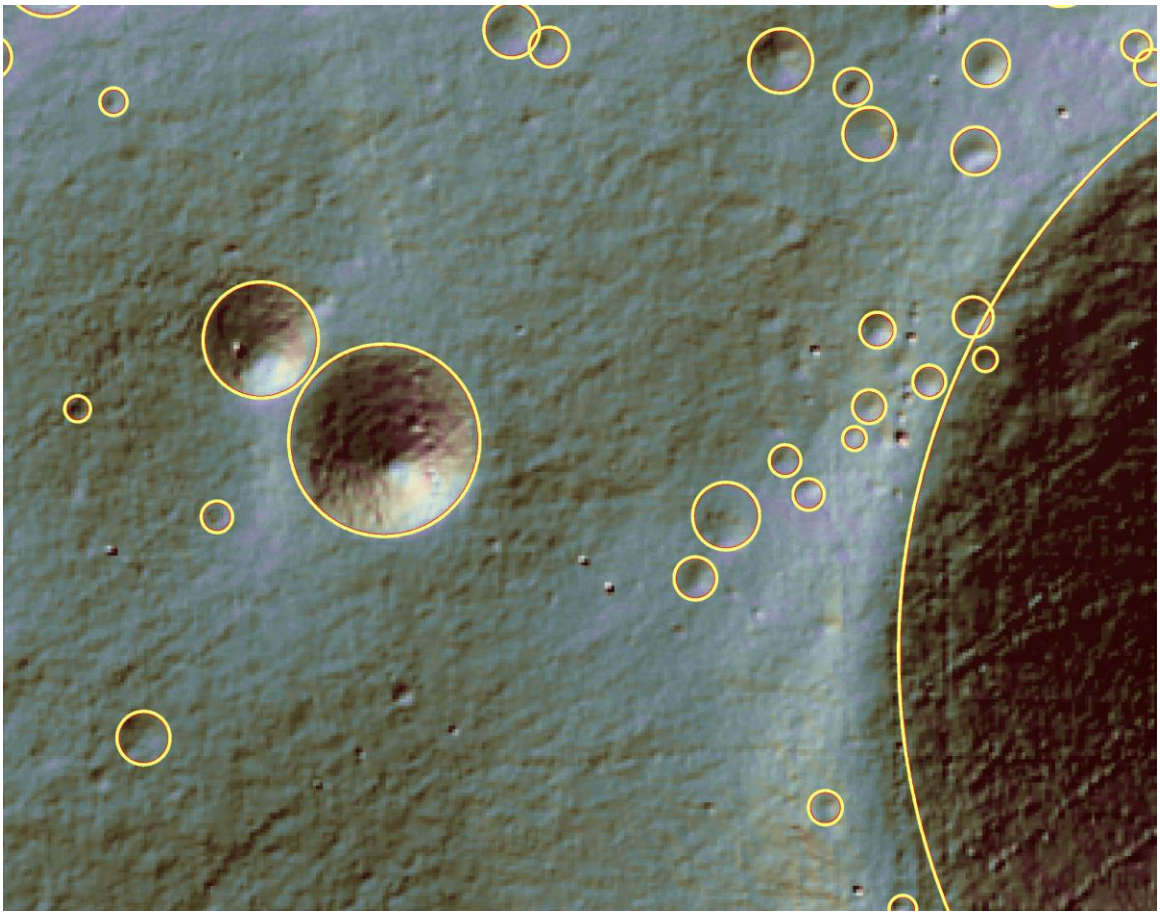

Figure 5: Map illustrating the crater counts and rim buffers in the wall region of Faustini (84.8ºE, -87.23ºN) using ArcMap 10.7.1 and CraterTools. At this scale we can see the crater emplacements clearly, illuminated by the Hillshade overlay mimicking the Sun's light at an angle of 30 degrees.

With the rim buffers created, I used the Add Surface Information (3D Analyst) Tool to calculate the average slope of the buffers. Once this was done, the crater buffer attribute table was exported as a text file to further manipulate into plots using Python. This process was completed 16 times for each of the crater counts collected in the complex craters included in this study. The initial approach used the rim-buffer attribute table data containing the rim-buffer slope information, diameters, and (x,y) coordinates for the crater count..

Potential issues would be buffer areas may be within the counted crater, meaning that the buffer area may contain the slope within it and thus the slope variation does not represent the

actual crater wall; therefore, we conducted several tests to see whether the buffer areas properly contain the wall slope. Several buffer cases were performed: 20 m (considered in Figure 4), 100 m, and 500 m shown in Figure 6.

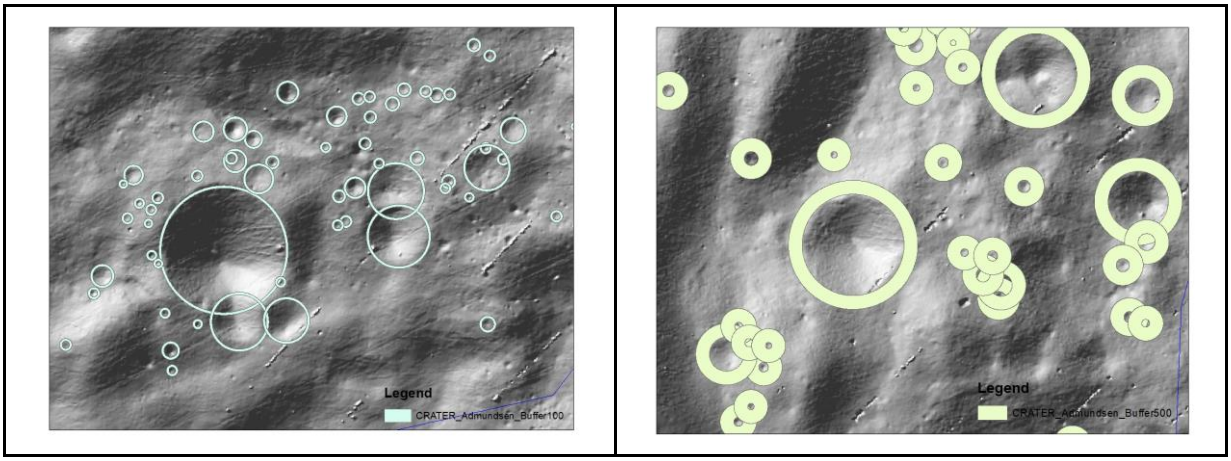

Figure 6: Rim buffer thicknesses of 100 m (blue) and 500 m (green) using Arcmap 10.7.1, CraterTools (Kniessl et al., 2011), and the Buffer (Analysis) Tool.

These buffer size classes were determined by the size distribution of the craters analyzed on the walls. The range in crater sizes from sub-kilometer to 35 km was enough variation to use this buffer size range. By using wider buffers, we were able to account for as much of the exterior of the crater emplacement as possible. This gave the most promising results on analyzing the slope conditions of the emplacement. However, potential issues also arise with increasing crater-buffer sizes. The first, is that the buffer still may not be large enough to account for the material truly outside of the entire crater emplacement. This falls under the issue that crater emplacements are not perfect circles. The next issue is that within the largest crater-buffer size (500 m), the smaller craters found in close spatial relation to one another may experience buffer overlap. This is where the buffer of one crater emplacement encounters or completely covers another crater

emplacement. This scenario would have the original crater buffer considering the slope of the interior of another crater, and not the complex crater wall.

2.2 Lack of craters greater than 1km

From this analysis, it was noted that crater populations greater than 1 km in diameter were significantly depleted on the walls of complex craters. This finding was justified to be the effect of landslides from meteorite bombardment on the walls. This event is size dependent and would have to be large enough to generate enough energy to induce mass movement of material on the walls. Leading to interpretations that this is why these crater populations are missing. The landslide movement is responsible for the partial or total erasure of these crater emplacements.

The crater counting analyses spanned 8186 counts over a combined area of 34,926.232km^2 (Table 1). With these counts, we created histogram plots to illustrate the variations in crater diameter populations shown below in Figure 7.

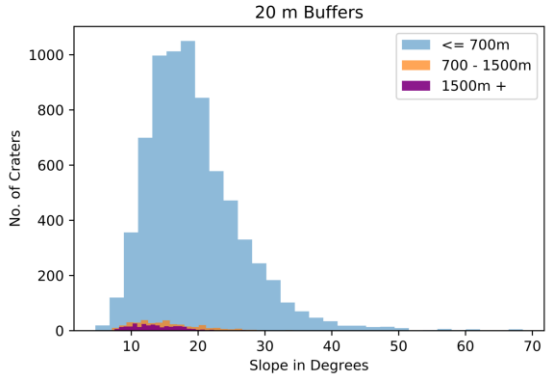

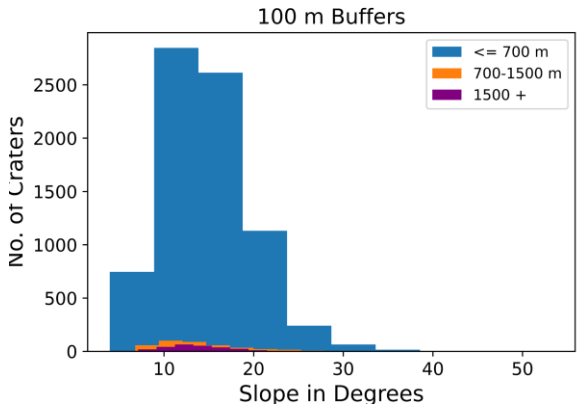

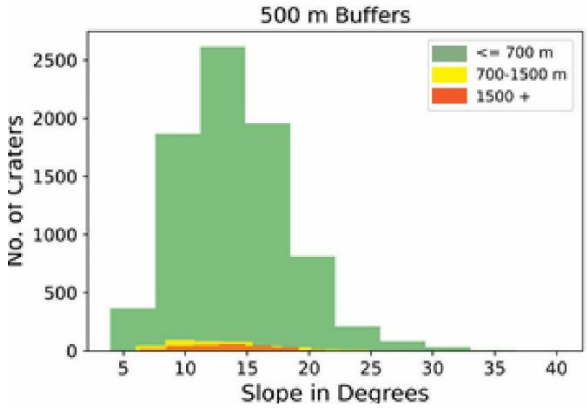

Figure 7: Histogram plots showing the number of craters found within each size bin. The first histogram used 20 m buffers. The second histogram used 100 m buffers. The third histogram used 500 m buffers. The mode crater size analyzed remained in the > 700 m crater population bin.

From this result we see the most common crater population is within the 700 m or lower bin.

Within this bin alone are 7251 craters. It is important to also notice that this population has

varying slope conditions and are found at very shallow (5°) and steep (69°) slope conditions. This result confirms the hypothesis that the most common crater population on the walls belongs to the smaller craters, as their impactors do not possess enough energy to induce landslides. Further investigations were completed using cumulative size frequency distribution (CSFD) plots (Figure 8). These plots illustrate how many craters are distributed per unit area as a function of crater size (diameter).

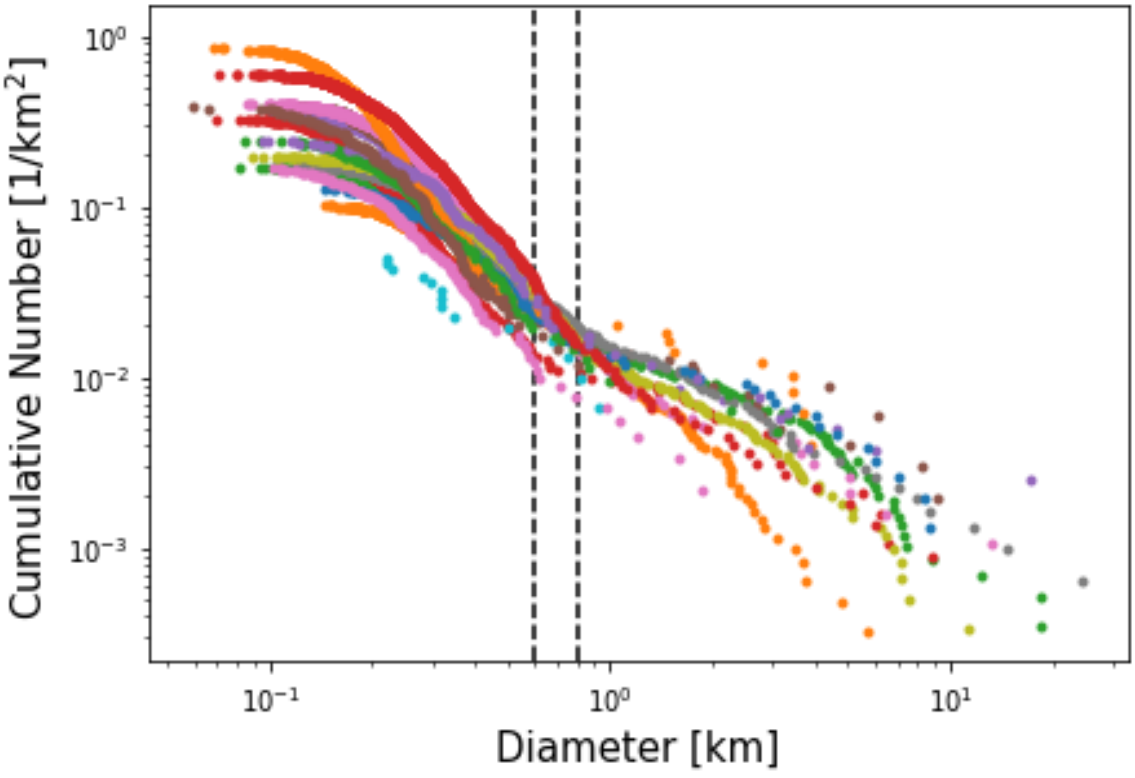

Figure 8: Crater Size Frequency Distribution plots (CSFDs) of craters on the walls of the 16 complex craters around the lunar south pole. The vertical dashed lines give the 600-800 m transition.

The combined CSFD plot shows a distinct transition between crater populations less than 600 and greater than 800 m in diameter. This can be observed in our plot by the reduced number of craters greater than this transition. This transition is due to landslide erasure of these crater

emplacements, while the craters in the smaller population do not have enough energy to induce landslides. This interpretation implies that the degradation of complex crater walls may be more affected by impactors capable of forming emplacements > 600-800 m. This differs from earlier work as these craters are solely found on the walls of complex craters, rather than the floors.

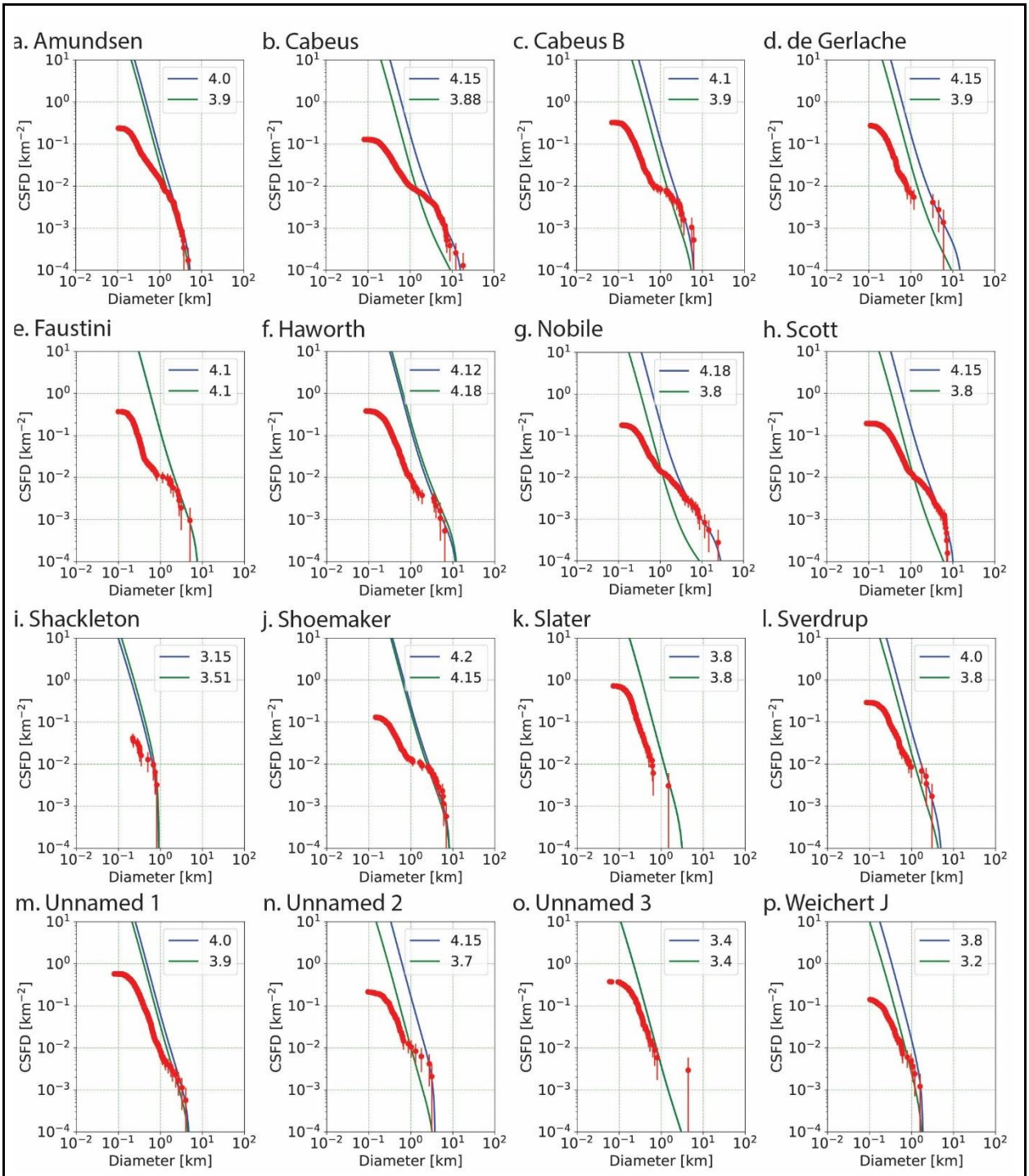

Figure 9: The individual CSFDs of the 16 complex craters found within our analysis. The Red dots with error bars indicate the crater counts for each complex crater. The blue line indicate the Neukum model age based on our counts. The green lines indicate the model age as derived from Deutsch et al., (2020), Tye et al., (2015), and Cannon et al., (2020).

By separating the combined CSFD into their individual plots, this allows for the analysis of transitions within crater populations for each complex crater. Shown in Figure 9, distinct transitions in all crater populations can be shown in all except for Amundsen. We used the crater count data on the walls to compute each CSFD (Appendix). In addition, the model ages for each complex crater were used to plot along with the Neukum Production Function (NPF) (Deutsch et al., 2020; Tye et al., 2015). Notably, the NPF's do not properly align with the crater populations. Giving the interpretation that craters on the sloping walls do not accurately follow the NPF for the complex crater. This is likely due to the enhanced crater erasure process on the walls due to landslide events from impactors.

In the cases where the NPF significantly did not properly follow model ages derived from Deutsch et al., 2020, Tye et al., 2015, and Cannon et al., 2020, the determined new model ages given as the blue lines within Figure 9. The largest gap within previously determined model ages and the crater counts model ages are shown in Cabeus, de Gerlache, Unnamed 2 and Weichert J. In Deutsch et al., 2020 and Cannon et al., 2020 the model ages for Cabeus, de Gerlache, Nobile, Scott, Sverdrup, Unnamed 2 and Weichert J are 3.88, 3.9, 3.8, 3.8, 3.7, and 3.2 respectively. For instance, Scott originally was characterized by having a Neukum model age of 3.8 Gyr (Deutsch et al., 2020). Through this crater counting analysis on the walls, there were noted more craters than originally obtained (Deutsch et al., 2020). In their study, they only counted regions with slopes $< 10°$ and over an area of < 100 km^2 of the complex craters while this study only counted the sloping walls.

To compare this result, craters on the floors were counted on four complex craters and plotted the CSFDs in comparison to the CSFDs of the walls. These plots are shown above in Figure 10.

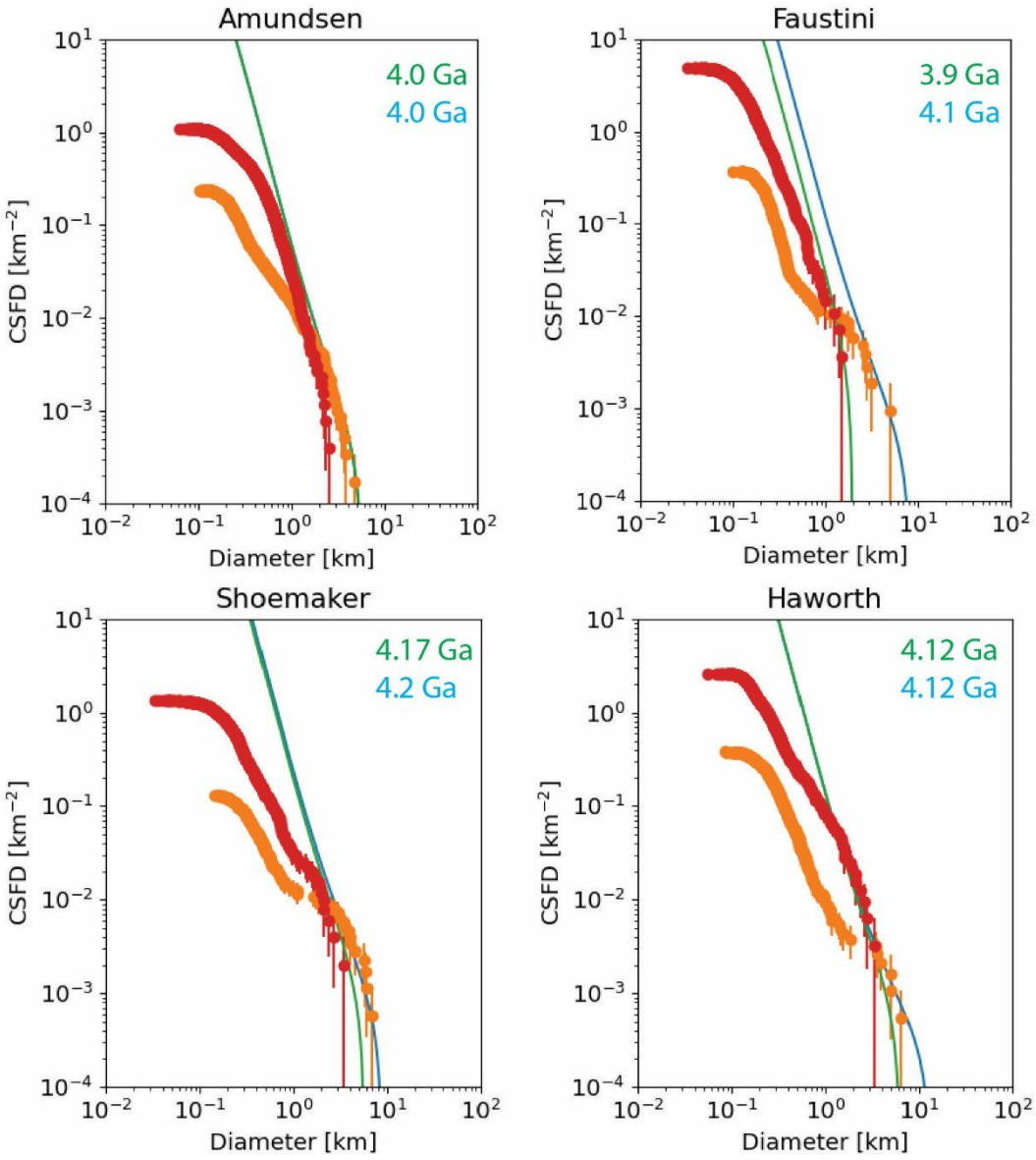

Figure 10: Crater Size Frequency Distribution Plots (CSFDs) of Amundsen (A), Faustini (B), Haworth (C) and Shoemaker (D). The orange CSFDs represent the floor counts. The green PF lines represent the age given by the floor counts. The blue PF lines represent the age given by the wall counts. (Neukum et al., 2001). Floor counts completed by P. Montalvo.

By doing this, there is confirmation that the Neukum model ages for the included craters are consistent with those determined from the wall counts.

3. Magnitude of topographic diffusion on complex craters

Discussions on how topographic diffusion has influenced the complex craters investigated in Section 3. To quantify this process, first this study defines the erosion depth on the wall and the accumulation depth on the floor. Note that the erosion depths of the examined complex craters used help us derive the resurfacing rate given in Table 1.

3.1. Formulation of erosion and accumulation depths

First was the computation of the erosion depth on the wall and the accumulation depth on the floor. This study operates under the assumption that after the emplacement of a complex crater, the excavated region on the wall is removed, and the erased crater volume is then equally added to the floor. This composes the accumulation volume. To compute the total erased crater volume, it was considered that the difference between the total number of crater emplacements and the present visible crater number would give the total number of erased craters. The total emplaced crater number was determined by using the Neukum crater generation model (Neukum et al., 2001).

Figure 11 shows the schematic of the present approach to determine the difference between the total number of craters emplaced and the visible crater number at present. First, the cumulative crater data was used to determine a smooth approximated function. For this, this study applied Neukum's logarithmic polynomial function (Neukum et al., 2001; Neukum, 1983), which is given as:

$$log_{10}(N) = \sum_{j=0}^{n} a_j \, \mathrm{x} \log_{10}(D)^j \quad (2)$$

where N is the cumulative crater number, a_j is a scalar parameter for an index of j, and D is the crater diameter. Using this polynomial function instead of empirical data mitigated issues with obtaining the crater numbers at a given diameter with well-sorted crater diameter intervals. This later limits the integral calculation for the total erased crater volume. Using a least square approach, the best set of a_j was computed for the polynomial function to describe the empirical data. n defines the total number of the polynomials and is usually defined as 11 in the Neukum form (Neukum et al., 2001). However, it was decided to make it flexible in this model to avoid overfitting issues. It was determined that $n = 10$ would be a suitable setting for this problem. Next, was to calculate the differential value, $-dN/dD$, for the crater number at a given crater diameter. The negative sign gives a positive value as the slope of N is always negative (see the details for Hirabayashi et al., 2017). The advantage of this process is that the derived values of a_j can be directly used for $-dN/dD$ (Neukum et al., 2001). This study used the sets of a_j for the Neukum model with a proper model age and the visible crater number on the wall to determine N and $-dN/dD$ for them.

Next, was the determination of the difference between the $-dN/dD$ value for the Neukum model and that of the visible crater number on the wall (the shaded region in Figure 11b). The total crater volume erased from the wall, V, is now given as:

$$V = \int_{Dmin}^{Dmax} -\frac{dN}{dD} v(D) A_w dD \quad (3)$$

where $v(D)$ is the excavation volume generated by a single emplacement of a simple crater with a diameter of D. Considering that the final excavation depth is about 10 % of D yields the excavation volume as:

$$v(D) \sim \frac{1}{15}\pi D^3 \quad (4)$$

After obtaining V, the eroded depth over the wall and the accumulated depth on the floor was determined. For this, the floor area, A_f, and the wall area, A_w were used. The eroded depth on the wall is defined as $h_w = V/A_w$, and the accumulation depth is defined as $h_f = V/f$.

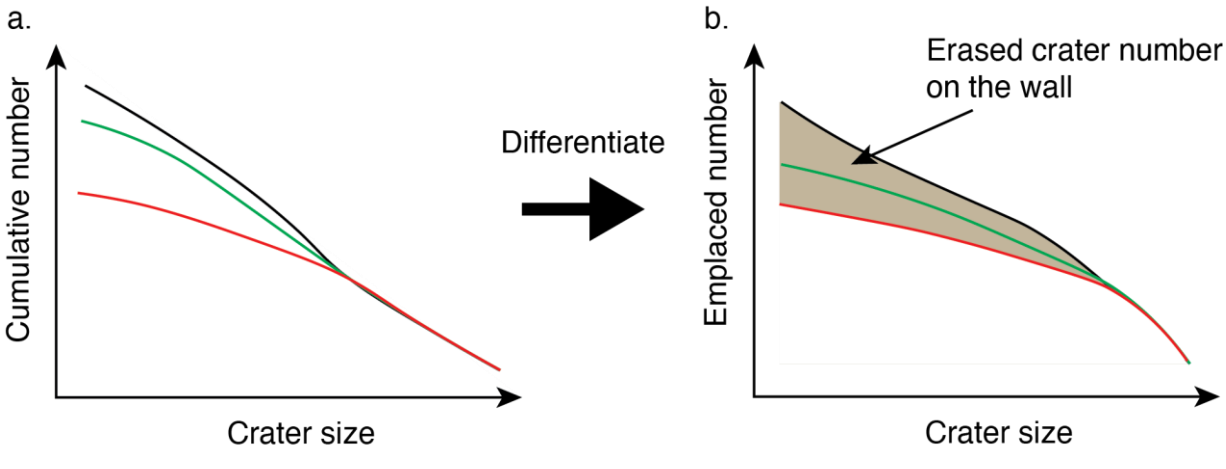

Figure 11: Schematic of computing the number of erased craters on a crater wall. The black line is the Neukum model, the green line is the visible crater number on the floor, and the red line is the visible crater number on the wall.

The purpose of this approach is to roughly determine the total volume erased on the wall from impact induced landslides and accumulated on the floor; however, there are many uncertainties. Therefore, interpretation of these results cannot be taken without caution. First, the assumption was made that the considered complex craters were affected mainly by primary craters (i.e., craters made by meteoroid impacts). However, it is likely that secondary craters, or craters made by re-impacts of ejecta from primary craters, affected these regions, too. If this is the case, it is necessary to use a proper crater production model (Costello et al., 2019). Note, the baseline study is Deutsch et al. (2020) and Tye et al. (2015), who considered craters within the complex craters to be primaries and calculated the model ages. The present study followed their settings. Second, the wall may experience crater equilibrium, where the number of crater erasure apparently equals that of crater emplacement. If this is the case, the currently visible crater

number on the wall may not provide the actual number of erased craters (Hirabayashi et al., 2017). However, because such a mechanism on a sloping surface is not well constrained, this work does not consider this issue and leave it as a future investigation. These issues raise a possibility that the wall might have more craters erased than considered in this study, leading to an interpretation that our approach would give lower bounds of h_f and h_w. Finally, we did not use the visible crater number on the floor to determine the total erasure volume on the wall because it is likely that craters on the floor may be erased by crater emplacements or mass movement from the wall.

3.2. Diffusive speed of lunar south pole complex craters

Using the total amount of mass wasting and ages derived previously, allows for the calculation of the diffusive speeds for the complex craters. This work used the diffusive equation to characterize topographic diffusion and its speed (Fassett and Thomson, 2014). Below, is the determination of the degradation state, κt, an integral of the diffusivity over time, used to quantify the diffusive rate of each complex crater.

The size dependence of κt exhibits two distinctive trends. First, the κt values of craters smaller than ~30 km in diameter are aligned along the scaling relationship for simple, bowl-shaped craters (Fassett et al., 2018). Second, those of craters larger than ~30 km in diameter are two orders of magnitude higher. The size dependency slope power in this diameter range is determined as 1.05, which is consistent with that derived by earlier empirical work, i.e., ~0.92 (Fassett et al., 2018). These two trends can also be explained by age. Those having higher degradation states are all Nectarian and pre-Nectarian craters. Those trends infer a transition from a lower degradation trend (solid line) to a higher degradation trend (dashed line). Note that

work suggested that the κt value's size dependence at ~5 km crater diameters may be less than smaller craters (Fassett et al., 2018), which apparently contradicts our results. A possible explanation may be limited data samples in the ~5 km diameter range (Fassett et al., 2018).

The derived κt suggests a significantly higher degradation process on the considered complex craters than that predicted for simple craters (Figure 12c and 12d). The dimensional κt values are multiple orders of magnitude higher than those for small craters (Fassett and Thomson, 2014). Figure 12d also displays the κt corrected by the size dependency described in Figure 12c. Both scaling relationships cross each other at 3.4 Gyr, but the one for complex craters rapidly increases before that age. Note, the scaling relationship found by Fassett and Thomson (2014); Fassett et al., (2018) only applies up to an age of 3.8 Gyr.

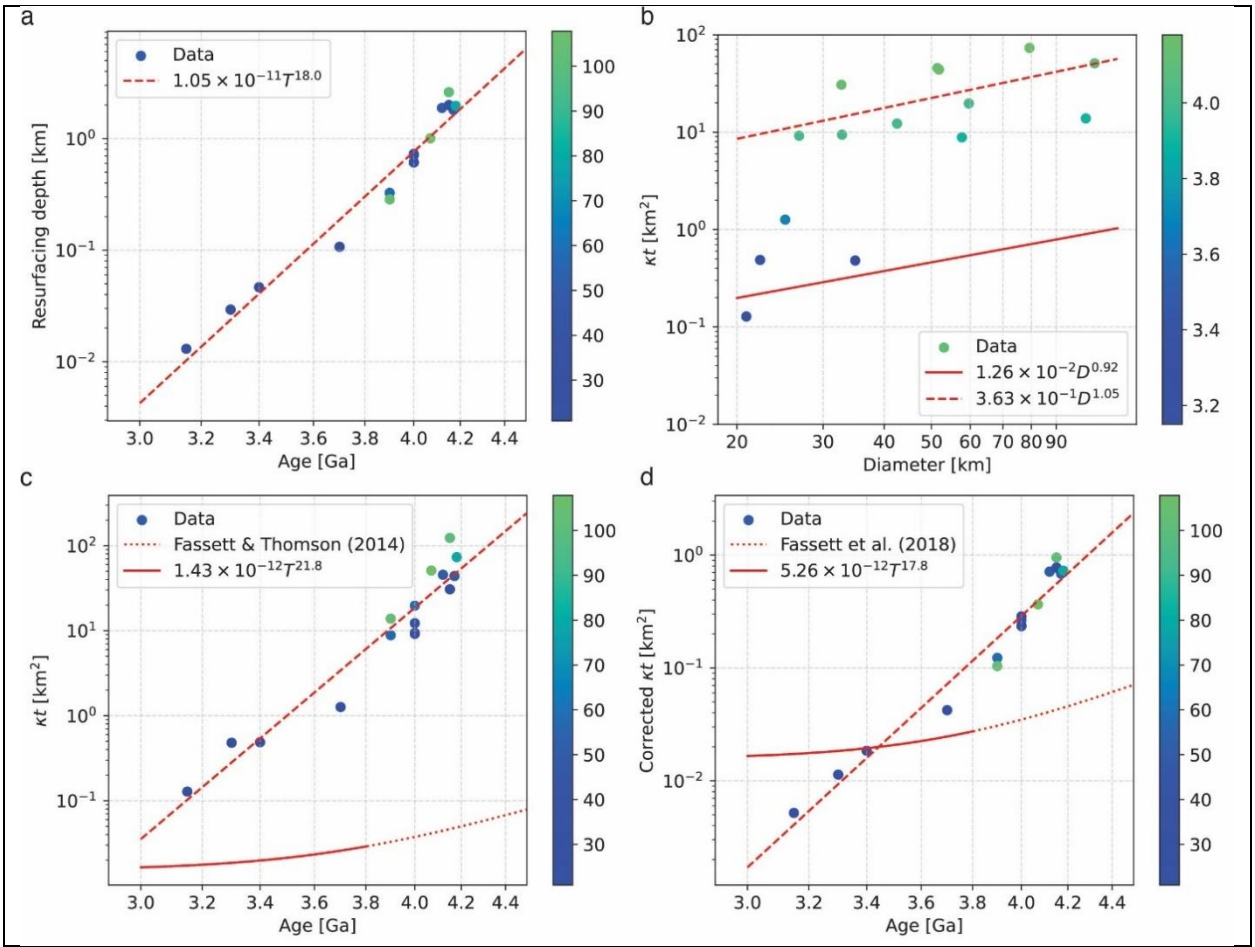

Figure 12: Resurfacing of the 16 complex craters near the lunar southern pole. Panel a shows the resurfacing depth as a function of age. The color map describes the crater diameter variation. The dashed line is a scaling relationship. Panel b gives the size independence of the κt value as a function of the crater diameter. The solid line shows the scaling relationship for small, simple craters less than 5 km in diameter (Fassett and Thomson, 2014). The color map is the Neukum-based model age. Panel c shows the variations in the κt value with age. Panel d illustrates the κt value corrected by the size dependency given in Panel b. The color maps of Panels c and d represent the crater diameter. For Panels c and d, the results by Fassett and Thomson (2014); Fassett et al., (2018) are only applicable to the ages less than 3.8 Gyr.

4. Discussion

Understanding the evolution of surface roughness of the moon gives us insight into the ages of crater populations. The younger crater populations are more defined, becoming smoother and less rocky over time (Wang et al., 2020). Lunar surface roughness is not constant throughout the body. Rosenberg et al. (2011) found that the lunar highlands and mare regions are contrasting greatly in roughness properties. The lunar highlands are rough and old, and exhibit are densely covered by craters while the Mare regions are considered to be young due to their less cratered conditions (Wang et al., 2020).

Also, this analysis may be able to give strong insights into the impact flux on the moon (Head et al., 2010; Fassett and Thomson, 2014; Fassett and Minton, 2013). Crater counting is one of the processes to constrain the impact flux; however, because of crater erasure processes, the true impact flux is currently unknown. It is considered that in many areas on the moon, the crater production and erasure are currently balanced, meaning that the crater population is apparently constant. This phenomenon is called crater equilibrium (Gault 1970). Modeled production functions show the elevated number of small lunar craters to be consistent with the high production of regolith over the last ~ 1 Ma (Xie et al., 2019). A better understanding of crater degradation can constrain the true impact flux over the history of the Moon.

Crater populations are distinguished by their size and morphologies. These populations range from the smallest craters known as microcraters, followed by mid-range simple craters, and finally the largest complex craters. Microcraters start at 1μm in diameter and are caused by high-velocity impacts of particles of cosmic dust. Simple craters have a larger size range than microcraters, and are defined by their bright ejecta deposits, circular raised rim, and steep sloping walls near the rim. Finally, complex craters are found within the largest size range and

have similar features to simple craters but are differentiated by the presence of a flat floor, central peaks, and terraces (Melosh, 1989).

To achieve the defined objective, the calculated erosion results were compared with those of Fassett and Thomson, (2014) to quantify how fast complex craters are degraded by topographic diffusion. Importantly, note that the degradation rate may change depending on the crater sizes and through the complex crater's impact history. The larger the crater size is, the longer the topographic diffusion time scale becomes. The diffusion coefficient representing the factor of diffusion, kappa, tends to be high within recent history (< 1 Ga) and similarly at the early stage of the Moon (> 3 Ga). This recent high kappa value may give two implications: a recent higher impact flux (Fassett and Thomson 2014) or a higher degradation process of fresh, young craters (Fassett and Thomson, 2014).

Over time the crater walls found on complex craters are subject to impact events which change their morphologies. This change affects the topography and original crisp features become eroded because of small crater emplacements. This is known as topographic diffusion. The original concept of topographic diffusion investigates asymmetric ejecta emplacements on sloping surfaces (Ross, 1968; Soderblom, 1970; Fassett and Thomson, 2014). This work calculates the diffusion rate of complex craters by using a mathematical model. Assuming that the average diffusivity is spatially the same over one complex crater, which is also assumed to be axisymmetric along the crater center, the diffusive equation in the given cylindrical coordinate frame (r, ϕ) is given as (Fassett and Thomson, 2014):

$$\frac{\partial u}{\partial t} = \frac{\kappa}{r}\frac{\partial u}{\partial r} + \kappa\frac{\partial^2 u}{\partial r^2} \qquad (5)$$

Where r is the position along the radial direction, u is the resurfacing height, and κ is the average diffusivity. The first term represents the influence of the slope on the resurfacing height, while

the second term describes how the curvature affects that height. With multiple assumptions, this work analytically determines the degradation state, an integral of κ with respect of time given as:

$$\kappa t = \int_0^t \kappa dt \quad (6)$$

Given the limited data points in this research (16 complex craters), the initial topographic profiles are not strongly constrained in a statistical way. Particularly, it is noted that the morphologies are likely different for each crater (Kalynn et al., 2013). To roughly estimate the degradation state, the assumption was made that the slope term and the curvature term in eq. 5 are apparently similar, thus giving:

$$\frac{1}{r}\frac{\partial u}{\partial r} \sim \frac{\partial u^2}{\partial r^2} \quad (7)$$

By rewriting the equation this way, deriving:

$$\frac{\partial u}{\partial t} \sim \frac{2\kappa}{r}\frac{\partial u}{\partial r} \quad (8)$$

This equation is simplified to discuss the scale of the resurfacing height, i.e., the height of mass wasting accumulation. The crater wall is circularly distributed away from the crater center. Using this trend, $r \sim R$ is approximated, where R is the crater radius and thus $D/2$. Considering that the slope is described using the slope angle, Θ, obtaining:

$$\frac{\partial u}{\partial t} \sim \frac{2\kappa \tan\Theta}{R} \sim \frac{4\kappa \tan\Theta}{D} \quad (9)$$

Followed by integrating over the age of each crater yielding:

$$u \sim \int_0^4 \frac{4\kappa \tan\Theta}{D} dt - \frac{4\kappa \tan\Theta}{D} \quad (10)$$

For the slope conditions, 28.2° was used as the average slope angle. Eventually, it is determined the degradation state as $\kappa t - 0.47uD$, respectively. Note, that the focus is on discussing the orders of this parameter but not providing precise values. The average value was used while being aware of the variation of the slope angles. However, the slope only affects the resurfacing depth

with a factor of tanΘ, 2.4 at maximum for Shackleton as an extreme case, which does not change the orders and so does not change our conclusions.

This study used Deutsch et al., (2020) and Tye et al., (2015) as a baseline for the crater counting approach. By analyzing complex crater degradation, I defined the craters that have landslide material covering their entire floors versus those that do not. By doing this, the determination can be made on how degraded each complex crater is. Looking at the counts done by Deutsch et al., (2020) and Tye et al., (2015), below is a comparison of the area they considered to be the wall and floor regions. Haworth, Shoemaker, Shackleton and Unnamed 3 were consistent with regions determined to be the floor and wall. Unnamed 1 has landslide material included within the wall region, but not the floor. There are some inconsistencies seen in Cabeus B, as they only measured one region on the floor to do their counting, not the entire floor. There is evidence for potential landslide material throughout the floor. This landslide material can be traced back to fresh sloping regions on the walls. de Gerlache is an interesting case, as it has a very large emplacement that takes up roughly 1/4th of the complex crater. Deutsch et al., (2020) counted higher within the wall regions, however, to maintain consistency I similarly chose to exclude the large emplacement. Within de Gerlache determined that there is landslide material considered within the wall regions. Nobile has evidence for landslide material within the floor region, and similar to de Gerlache, also has a large emplacement taking up a portion of the crater. I included this emplacement within the crater count analysis, as it was determined that the emplacement itself made up a portion of the overall complex crater wall. There were some initial inconsistencies seen in Slater, but the counts have since been adjusted to be consistent with the regions Deutsch et al., (2020) identified. Scott has a much smaller counting area in Deutsch et al., (2020) than what was observed as the floor in this work. By the

definition used here, the floor may still include some landslide materials. These can be seen along the left boundary between the wall and floor. For the measurement of Sverdrup, only about ½ of the floor was considered in Deutsch et al., (2020). This work included the other half as the wall region, as it fits the definition of having a slope > 10º. Unnamed 2 has evidence for some landslide materials on the floor, but the floor is not totally covered by landslide material. This can be seen in the upper region of the boundary between the floor and wall. Within Cabeus, Deutsch et al., (2020) only looked at one region on the floor. The large impact craters were included within the counts as they fell within < 10° slope conditions. There is potential landslide material seen on the left boundary between the floor and wall. Weichert J has a terrace, which Deutsch et al., (2020) considered for their analysis. This study included this region as a portion of the wall. Landslide material can be seen on the lower right and center portion of the floor. The evidence for this is seen in the steep slope on the wall adjacent to this material. Though Shackleton was consistent with regions considered in Deutsch et al., (2020), it was noted that there are some landslide materials seen on the left and right sides of the boundary between the floor and wall. The right side is more prominent, and included in the wall region, while the left is more faded, and was ultimately excluded from the wall. Finally, looking at Amundsen, Deutsch et al., (2020) considered a different counting region.

Though it has not been discussed within this manuscript, the presence or lack of volatiles, namely, water ice found within these complex craters may alter the degradation seen in the results. Remote sensing observations have distinguished the presence of lunar water ice or other volatiles present within and near the lunar southern pole (Lucey et al., 2021). This finding has sparked an ongoing research effort to learn how and where its origins were, harvesting mechanisms, or even calculate how much ice is present under the surface. NASA's ongoing

Volatiles Investigating Polar Exploration Rover (VIPER) mission is in the business of doing just that. Potential water sources include meteoroid and comet impacts (Ong et al., 2010), solar wind implantation (Hurley et al., 2017), and volcanic outgassing (Needham and Kring, 2017; Head et al., 2020). Water delivery to the Moon's surface was likely more active within the early history of the Moon rather than the present due to a higher rate of asteroid and comet impacts and enhanced volcanic outgassing. However, other processes that compete with this include impact mixing (Costello et al., 2021) and thermal destabilization (Siegler et al., 2015; Martinez and Siegler, 2021) that may have redistributed water over time. That being said, the presence of ice has the potential to alter surface or subsurface properties within these regions.

4.1 Mixing of ancient water with mass movement materials

Topographic diffusion on a large complex crater enhances material transport from its wall to the floor. This process mixes water with regolith in two ways. First, water may be mixed with regolith on the wall when a series of mass wasting occurs. Second, such transported materials now overlay accumulated water layers on the floor. In contrast to impact mixing, which may induce heat and thus water ice sublimation (Costello et al., 2021), mass wasting may not give water a significant heat, and thus materials may overlay water layers without sublimation.

Considering these mixing mechanisms, rough estimates of the average water fraction within accumulated landslide materials on the crater floor are determined. The water fraction is defined as a ratio of the amount of water supply to that of accumulated materials in a unit area over time. To focus on ancient water, we compute the mixture of water ice over 3.0 Ga to 4.2 Ga. The average depth of the accumulated mass wasting on a crater floor in a unit area is given as the

scaling relationship in Figure 2, i.e., $u = 1.05 \times 10^{-11} t^{18}$ for 3.0 Gyr to 4.2 Gyr, where t is the time in Gyr.

Better capturing how water has been trapped in cold regions, i.e., cold trap, (Prem et al., 2015, 2018, 2019) is beyond the scope, though earlier work suggested that imparted water molecules might widely be distributed as part of the exosphere over the Moon (Prem et al., 2015, 2019). Such a condition may lead to relatively homogeneous water accumulation over cold regions, if their thermal conditions are met (Siegler et al., 2015). Based on this scenario, the water supply density was calculated, i.e., water deposition over a unit area, or 1 m^2, by dividing the total water delivery amount by the lunar area, ~40 Mkm^2. Note, this study accounts for three sources of water supply in a PSR. The first source is solar wind, and its contribution to water generation over the entire lunar surface over 1 Ga is 5×10^{11} kg/Ga (Hurley et al., 2017), giving its density as 1.38×10^{-2} kg/Ga/m2. The second source is asteroids and comets. The water delivery rate over 1 Ga is 2.5×10^{15} kg/Ga, and its density is 66 kg/Ga/m^2 (Ong et al., 2010). The last source is volcanic outgassing, which may have delivered 1×10^{14} kg of water, equivalent to 2.6 kg/m^2 in total, to the lunar surface during the Imbrian (Needham & Kring, 2017; Head et al., 2020).

The calculation of the water supply variation employs the following assumptions. First, water delivered by solar wind is supplied constantly. This assumption may oversimplify the model as earlier study suggested a possible variation over the lunar history (Borg et al., 1980). However, as discussed below, the effect of solar wind is trivial compared to other sources, particularly asteroids and comets. Second, volcanic activity-driven water is supplied equally during Imbrian. Third, the water supply made by asteroids and comets is proportional to their impact fluxes and so determined applying the Neukum chronology model (Neukum et al., 2001).

Note that the comet impact flux may be significantly different from but should be much less than the asteroid flux (Morbidelli et al., 2018). Again, however, because the contribution of asteroids is so significant that the influence of comets is almost negligible.

The results show that the water fraction ranges between ~0.1 wt% and ~2 wt% over 4.2 Ga to 3.2 Ga, which is similar to the water fraction observed on the lunar surface (Hayne et al., 2015; Li et al., 2018). There are two notes. First, while in computing the average water fraction, episodic mass wasting events may induce stratigraphic water layers over accumulated materials, similar effects to ejecta blanketing (Cannon et al., 2020). This implies that the water distribution may be locally heterogeneous along the vertical direction. Second, the analysis does not consider the effect of ejecta blankets from the outside of craters. Overlaps of large ejecta blankets may have created a hundreds of-meter-thick layering structure (Cannon et al., 2020). If this is the case, these large ejecta blankets likely mix existing mass wasting materials. Thus, pre-Nectarian and Nectarian craters are likely candidates that are significantly affected by such large crater ejecta blankets. However, as discussed later, because of internal heat and impact mixing, these old craters are ruled out from the candidate regions that may host ancient water in shallow subsurface layers. In other words, the consideration of large crater ejecta blankets does not affect the conclusions about the ancient water preservation.

4.2 Internal heat and impact mixing contributing to water distribution

In addition to mass wasting mixing water with regolith on crater walls and floors, impact mixing and internal heat may redistribute water in subsurface layers. This section argues how these processes contribute to the existence of the ancient water. First was the incorporation of impact mixing over time proposed by analytical work (Costello et al., 2021). Following this, was the application of the in-site reworking zone, a region above the bottom of saturation excavation

and burial by secondaries, which may interpret that subsurface water may not exist (Costello et al., 2021). Unlike topographic diffusion driven material accumulations that are assumed not to affect water thermally, direct impact cratering may induce enough heat to cause water sublimation within the crater cavity. Thus, regions within the in-site reworking zone may likely lack the water signature. The in-site reworking zone reaches up to 1 m at depth over 3 Ga (Costello et al., 2021). This work applied the depth variation of the in-site reworking zone's bottom as a function time over 3.2 Ga - 4.2 Ga. Next, the influence of internal heat on subsurface water had to be taken into account in order to determine the deepest region that water can be thermally stable. The thermal model developed by Hayne et al. (2017) was applied, which is incorporated into a finite element-based Newton Raphson implicit solver, to determine the subsurface equilibrium temperature. The internal heat is largely unknown particularly beneath the lunar south pole. Given this uncertainty, the Apollo heat flow measurement was incorporated (Langseth et al., 1976) to consider three heat fluxes 8 mW/m^{-2}, 16 mW/m^{-2}, and 32 mW/m^{-2} (Paige et al., 2010). Finally, allowing the computation of the subsurface equilibrium temperature distribution given three surface temperatures, 50 K, 75 K, and 100 K (Figure 13).

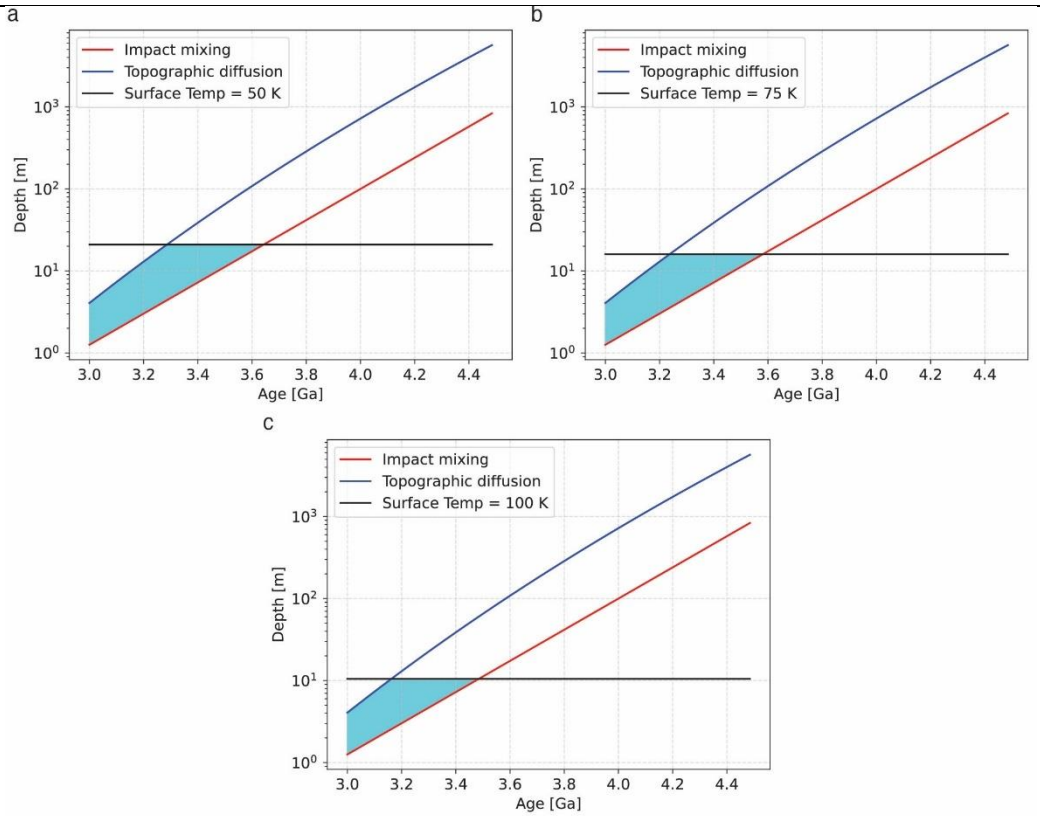

Figure 13: Presence of ancient water affected by topographic diffusion driven accumulation, impact mixing, and internal heat. For all of the panels, the red lines are the depth affected by impacts mixing, while the blue lines are the depth driven by topographic diffusion driven accumulation on a crater floor. The black lines describe the thermal threshold. The cyan regions are areas where ancient water may be preserved. Panels a, b, and c show cases when the surface temperatures are 50 K, 75 K, and 100 K, respectively.

Our purpose of employing this approach is to find the thermal threshold, the depth that reaches the water stability limit, i.e, 145 K, (Schorghofer, 2008). As seen below, the prediction of the thermal threshold reaches tens of meters in depth. This depth range is likely beyond the best estimates of the thermal properties that are covered by earlier work (Hayne et al., 2017; Martinez & Siegler, 2021). Given this limited constraint, it is assumed that the model by Hayne et al. (2017) provides reasonable thermal conditions in this depth range. Also, the 145 K thermal threshold defined here is set to be slightly higher than the water ice sublimation temperature, ~110 K. This is based on a hypothesis that the subsurface water ice may be stable at a

temperature as high as 145 K (Schorghofer, 2008). Furthermore, as Martinez and Siegler (2021) incorporated more comprehensive nonlinear effects of the thermal properties applicable to low temperature surface and subsurface layers, this analysis likely underestimates the thermal gradients, which gives deeper thermal thresholds. Finally, this study does not consider the influence of the lunar polar orientation on the polar thermal conditions, although it may have actively moved, changing the thermal conditions over the lunar history significantly (Siegler et al., 2015, 2016). If this is the case, the existence of ancient water may be affected not by the internal heat but by the sunlit condition, which would completely remove water beneath the surface. Figure 3 illustrates the conditions that ancient water could exist by avoiding interactions with those processes. The thickness of accumulated mass wasting on a crater floor is an upper bound of the ancient water existence as any regions beneath the original crater floor may have been highly affected by an intense heat during the formation of the hosting complex crater (lower side of the blue lines). A subsurface region deeper than the deepest depth of the in-site reworking zone allows water to exist (upper side of the red lines). However, the subsurface depth should be shallower than the 145 K thermal threshold to avoid a higher temperature (lower side of the black lines). All these factors constrain the ancient water existence conditions. Interestingly, depending on the surface temperature, there is an upper bound of the crater age that can host water that was delivered at a similar age. For example, if the surface temperature is 50 K (Figure 3a) water older than ~3.65 Ga may not exist. The 75K and 100 K surface temperatures prohibit the existence of water older than ~3.6 Ga and ~3.5 Ga, respectively (Figures 3b and 3c). This constraint on the crater age for the ancient water existence eases the potential influences of large ejecta blankets by Nectarian and pre-Nectarian craters (Cannon et al., 2020). Furthermore, if the surface is younger than 3.3 Ga (for 50 K), 3.25 Ga (for 75 K), and 3.15 Ga (for 100 K), the

ancient water distribution is bounded by the thickness of landslide materials. Considering the range of the internal heat (8 mW/m^2 - 32 mW/m^2), depending on the average surface temperature, ancient water older than ~3.6+0.2 −0.3 Ga is likely to be gone or highly affected by water at other ages.

4.3 Ages of highly degraded Nectarian and pre-Nectarian craters

Our study suggested that topographic diffusion-driven mass wasting may cause a resurfacing depth of ~1 km or deeper for craters older than 4.0 Ga. Because of the depth-to-diameter ratio of a simple crater on the Moon is roughly 0.2 on a flat floor (Melosh, 1989; Stopar et al., 2017), this depth becomes equivalent to the depth of a 5-km-diameter crater. The resurfacing process with this magnitude implies that craters less than 5 km in diameter formed on Nectarian and pre-Nectarian craters are highly degraded or buried and are now invisible. While this interpretation may be reasonable on average, it differs for each crater. Below, the heterogeneous nature of the degradation state based on their morphologies is argued.

Cabeus, Scott and Nobile are likely candidates that have experienced crater erasure at a diameter of ~ 5 km or less. These craters do not exhibit clear flat floors but have highly degraded surfaces (Figure 4). If their degraded morphologies result from topographic diffusion, craters less than 5 km originally placed on these craters are likely erased. However, these craters still host craters larger than that size, and our Neukum model ages are mainly determined based on these craters. Thus, the considered the derived ages of these craters are reasonable. Note, that if they are older than any other lunar south pole craters, they should be subject to large ejecta blanket emplacements (Cannon et al., 2020).

On the other hand, other Nectarian and pre-Nectarian craters such as Haworth, Shoemaker and Faustini have relatively clear floors (Figure 4). This study interprets that the central part of these floors have not been affected by mass wasting. Such materials first overlay the floor edges and are gradually transported toward the floor center. Thus, the amount of overlaying material accumulation is spatially different on each complex crater; the depth is deeper at the floor edges, while it is shallow or even zero around the floor center. This implies that the depth of mass wasting materials at the floor edges is deeper than the average accumulation depth. This contrast still allows a reasonable model age to be identified a for such a crater (Tye et al., 2015); Deutsch et al., 2020; Cannon et al., 2020), if the floors of their craters do not reach crater equilibrium at large diameters (Hirabayashi et al., 2017; Minton et al., 2019). For these craters, because our crater counting identifies that the floor-based model ages are similar to the wall-based model ages, the uncertainties are minimal.

4.4 Low size-dependence of complex craters' topographic diffusion

For craters larger than 30 km in diameter, the degradation state follows a scaling relationship proportional to $D^{1.05}$. This 1.05 slope power is consistent with earlier studies (Fassett et al., 2018; Riedel et al., 2020). On the other hand, earlier work also observed this reference slope power on the Moon (Basilevsky et al., 2018). Theoretically, the reference slope power defines an ideal situation when the degradation state becomes identical to geometric similarity (Minton et al., 2019). Thus, the degradation state less than 2 implies inefficient topographic diffusion; in other words, the actual degradation; in other words, the actual degradation state at present is less than that for the geometric similarity. Within the considered crater diameter range, larger complex craters are degraded by topographic diffusion less sufficiently than small

complex craters. This implies that larger ones can survive longer than those having geometric similarities. A possible contributor may be the variations in topography with size, contributing to how easily mass wasting occurs.

There was an observed apparent transition from the degradation state of smaller craters to that of large craters up to 30 km in diameter (Figure 12). If this is indeed a transition, there are two possible explanations. First, it is attributed to the crater size. The transition should occur at a crater diameter ranging between 5 km and 30 km, given earlier work that analyzed topographic diffusion of craters with 800 m and 5 km in diameter (Fassett et al., 2018). One possibility may be a complex-simple crater transition on the Moon, which is about 15 km (Pike 1977). If so, complex crater morphologies are more susceptible to large-scale mass wasting and thus have higher degradation states. However, they can still be visible because of their larger sizes. Second, this transition may simply result from the crater age, i.e., the level of bombardments to which the craters have been exposed, which is consistent with the trends of topographic diffusion of small craters (Fassett and Thomson, 2014; Fassett et al., 2018). If this is the case, this transition may suggest a shift of the bombardment trend at some time around 3.4 Gyr. Higher velocity impacts can induce higher destructive cratering processes, leading to large-scale mass wasting and thus a higher κt. This interpretation supports a hypothesis that an earlier bombardment phase (3.4 Gyr to 4.1 Gyr) may have been attributed to high-velocity impacts than a later lunar phase (Marchi et al., 2013). However, given our limited data samples, these discussions still lack a decisive conclusion and need further study.

5. Conclusions

In concluding this study, I now have a greater understanding of the crater populations on the walls of complex craters. I noted a distinct diameter transition at 600-800 m, promoting further investigations into what causes this. I deduced that the transition in crater populations is from impact induced landslides that cause total or partial erasure of the crater emplacements. Landslide material was first analyzed most clearly within the terrace regions of the complex crater. Notably in Amundsen (83.1E, -84.4N), terraces can be seen along the left side of Figure 1 within the complex crater. The mass movement of wall material leads to the accumulation of fine-grained sediment on the crater floor (Kumar et al., 2013). This study investigated the slope conditions for these crater emplacements by using different buffer sizes (20, 100, 500 m) and found little to no significant change in the results. The calculation of the erosion depth for complex craters was completed and noted there was a complementary relationship between complex crater age and erosion depth. This understanding along with the diffusion equation (Fassett and Thomson, 2014) was used to derive the timescale at which complex craters are affected by topographic diffusion. Further analysis was done on the role at which volatiles are present and affected by topographic diffusion by using a thermal model (Hayne et al., 2017) and determined that the effect of impact induced landslides has the ability to allow the subsurface to harbor water ice and give insights into these conditions.

6. References

Bandfield et al. (2017), Distal ejecta from lunar impacts: Extensive regions of rocky deposits, Icarus, 283, 282-299.

Borg, J., Chaumount, J., Langevin, Y., Maurette, M., Jouret, C., (1980), In: The Ancient Sun: Fossil Record in the Earth, Moon and Meteorites, Solar wind radiation damage in lunar dust grains and the characteristics of the ancient solar wind, pp. 431-436

Barker, M. K., Mazarico, E., Neumann, G. A., Zuber, M. T., Haruyama, J., Smith, D. E., A new lunar digital elevation model from the Lunar Orbiter Laser Altimeter and SELENE Terrain Camera, Icarus, Volume 273, 2016, Pages 346-355, ISSN 0019-1035, https://doi.org/10.1016/j.icarus.2015.07.039. (https://www.sciencedirect.com/science/article/pii/S0019103515003450)

Barker. M. K., Mazarico, E., Neumann, G. A., Smith, D. A., Smith, D. E., Zuber, M. T., Head, J. W., Improved LOLA elevation maps for south pole landing sites: Error estimates and their impact on illumination conditions, Planetary and Space Science, Volume 203, 2021, 105119, ISSN 0032-0633, https://doi.org/10.1016/j.pss.2020.105119. (https://www.sciencedirect.com/science/article/pii/S0032063320303329)

Basilevsky et al. (2018), Morphometric studies of the Copernicus and Tycho secondary craters on the Moon: Dependence of crater degradation rate on crater size, Planetary and Space Science 162, 31-40.

Boyce et al. (2020), The Tsiolkovskiy crater landslide, the moon: An LROC view, Icarus, Icarus 337, 113464

Brunetti et al. (2015), Large rock slides in impact craters on the Moon and Mercury, Icarus 260, p.289-300.

Burrough, P. A., and McDonell, R. A., 1998. Principles of Geographical Information Systems (Oxford University Press, New York), 190 pp.

Cannon, K. M., Deutsch, A. N., Head, J. W., & Britt, D. T. (2020). Stratigraphy of ice and ejecta deposits at the lunar poles. Geophysical Research Letters, 46, e2020GL088920. https://doi.org/10.1029/2020GL088920

Costello, E. S., Ghent, R. R., Lucey, P. G., (2021), Secondary Impact Burial and Excavation Gardening on the Moon and the Depth to Ice in Permanent Shadow, Journal of Geophysical Research: Planets, Vol. 166, e2021JE006933, doi:10.1029/2021JE006933

Craddock, R. A., & Howard, A. D. (2000). Simulated degradation of lunar impact craters and a new method for age dating farside mare deposits. *Journal of Geophysical Research*, 105, 20,387–20,402. https://doi.org/10.1029/1999JE001099

Deutsch, A. N., Head, J. W., Neumann, G. A., Analyzing the ages of south polar craters on the Moon: Implications for the sources and evolution of surface water ice., Icarus, Volume 336, 2020, 113455, ISSN 0019-1035, https://doi.org/10.1016/j.icarus.2019.113455. (https://www.sciencedirect.com/science/article/pii/S0019103519303689)

Eberly, D., 1999. Least Squares Fitting of Data (Geometric Tools, LLC), pp. 3.

Fassett, C. I., Head, J. W., Smith, D. E., Zuber, M. T., and Neumann, G. A. (2011), Thickness of proximal ejecta from the Orientale Basin from Lunar Orbiter Laser Altimeter (LOLA) data: Implications for multi-ring basin formation, *Geophys. Res. Lett.*, 38, L17201, doi:10.1029/2011GL048502.

Fassett, C., Minton, D. Impact bombardment of the terrestrial planets and the early history of the Solar System. *Nature Geosci* 6, 520–524 (2013). https://doi.org/10.1038/ngeo1841

Fassett, C. I., and Thomson, B. J. (2014), Crater degradation on the lunar maria: Topographic diffusion and the rate of erosion on the Moon, J. Geophys. Res. Planets, 119, 2255– 2271, doi:10.1002/2014JE004698.

Fassett, C. I. (2016), Analysis of impact crater populations and the geochronology of planetary surfaces in the inner solar system, *J. Geophys. Res. Planets*, 121, 1900– 1926, doi:10.1002/2016JE005094.

Fassett, C. I., Crowley, M. C., Leight, C., Dyar, M. D., Minton, D. A., Hirabayashi, M., Thomson, B. J., and Watters, W. A. (2017), Evidence for rapid topographic evolution and crater degradation on Mercury from simple crater morphometry, Geophys. Res. Lett., 44, 5326– 5335, doi:10.1002/2017GL073769.
Gault, D. E., "Saturation and equilibrium conditions for impact cratering on the lunar surface: Criteria and implications," in *Radio Science*, vol. 5, no. 2, pp. 273-291, Feb. 1970, doi: 10.1029/RS005i002p00273

Hartmann, W. K., & Gaskell, R. W. (1997). Planetary cratering 2: Studies of saturation equilibrium. *Meteoritics*, 32, 109–121. https://doi.org/10.1111/j.1945-5100.1997.tb01246.x

Hayne, P. O., Bandfield, J. L, Siegler, M. A., Vasavada, A. R., Ghent, R. R., Williams, J. P., Greenhagen, B. T. and others, (2017), Global Regolith Thermophysical Properties of the Moon From the Diviner Lunar Radiometer Experiment, Journal of Geophysical Research: Planets, Vol. 122, pp. 2371-2400, doi:10.1002/2017JE005387

Head, J. W., Fassett, C. I., Kadish, S. J., Smith, D. E., Zuber, M. T., Neumann, G. A., Mazarico, E., Global Distribution of Large Lunar Craters: Implications for Resurfacing and Impactor

Populations, Science, Volume 329, 2010, Pages 1504-1507, ISSN 0036-8075, doi: 10.1126/science.1195050. https://science.sciencemag.org/content/329/5998/1504

Head, J. W., Wilson, L., Deutsch, A. N., Rutherford, M. J., Saal, A. E., (2020), Volcanically induced transient atmospheres on the moon: Assessment of duration, significance, and contributions to polar volatile traps, Geophysical Research Letters, Vol. 47, e2020GL089509, doi:10.1029/2020GL089509

Hirabayashi, M., Minton, D. A., Fassett, C. I., An analytical model of crater count equilibrium, Icarus, Volume 289, 2017, Pages 134-143,ISSN 0019-1035, https://doi.org/10.1016/j.icarus.2016.12.032. (https://www.sciencedirect.com/science/article/pii/S0019103516304717)

B. Hofmann-Wellenhof, H. Lichtenegger and J. Collins, 2001. GPS - theory and practice. Section 10.2.1. p. 282.

Hoslapple, K. A., (1993) The Scaling of Impact Processes in Planetary Sciences, Annu. Rev. Earth Planet. Sci., Volume 21, ISSN 0084-6597, https://doi.org/10.1146/annurev.ea.21.050193.002001.

Hurley, D. M., Cook, J. C., Retherford, K. D., Greathouse, T., Gladstone, R. G., Mandt, K., Grava, C., Kaufmann, D., Hendrix, A., Feldman, P. D., Pryor, W., Stickle, A., Killen, R. M., Stern, S. A., (2017), Contributions of solar wind and micrometeoroids to molecular hydrogen in the lunar exosphere, Icarus, Vol. 283, 31-37, https://www.sciencedirect.com/science/article/pii/S0019103516300707

Johnson, B. C., Collins, G. S., Minton, G. A., Bowling, T. J., Simonson, B. M., Zuber, M. T., Spherule layers, crater scaling laws, and the population of ancient terrestrial impactors, Icarus, Volume 271, 2016, Pages 350-359, ISSN 0019-1035, https://doi.org/10.1016/j.icarus.2016.02.023. (https://www.sciencedirect.com/science/article/pii/S0019103516000907)

Kalynn, J., Johnson, C. L., Osinski, G. R., and Barnouin, O. (2013), Topographic characterization of lunar complex craters, *Geophys. Res. Lett.*, 40, 38– 42, doi:10.1029/2012GL053608.

Kokelaar, B. P., Bahia, R. S., Joy, K. H., Viroulet, S., and Gray, J. M. N. T. (2017), Granular avalanches on the Moon: Mass-wasting conditions, processes, and features, J. Geophys. Res. Planets, 122, 1893– 1925, doi:10.1002/2017JE005320.

Krishna, N., Kumar, P. S., Impact spallation processes on the Moon: A case study from the size and shape analysis of ejecta boulders and secondary craters of Censorinus crater, Icarus, Volume 264, 2016, Pages 274-299, ISSN 0019-1035, https://doi.org/10.1016/j.icarus.2015.09.033. (https://www.sciencedirect.com/science/article/pii/S0019103515004479)

Kreslavsky and Head (2012), New observational evidence of global seismic effects of basin-forming impacts on the Moon from Lunar Reconnaissance Orbiter Lunar Orbiter Laser Altimeter data, Journal of Geophysical Research, 117, E00H24.

Kneissl, T., van Gasselt, S., Neukum, G., Map-projection-independent crater size-frequency determination in GIS environments—New software tool for ArcGIS, Planetary and Space Science, Volume 59, Issues 11–12, 2011, Pages 1243-1254, ISSN 0032-0633, https://doi.org/10.1016/j.pss.2010.03.015. (https://www.sciencedirect.com/science/article/pii/S0032063310000887)

Kreslavsky, M. A., and Head, J. W. (2012), New observational evidence of global seismic effects of basin-forming impacts on the Moon from Lunar Reconnaissance Orbiter Lunar Orbiter Laser Altimeter data, J. Geophys. Res., 117, E00H24, doi:10.1029/2011JE003975.

Langseth, M. G., Keihm, S. J., Peters, K., (1976), In: Lunar Science Conference, Revised lunar heat-flow values, pp. 3143-3171, doi:10.1126/science.1187726

Li, S., Lucey, P. G., Milliken, R. E., Hayne, P. O., Fisher, E., Williams, J. P., Hurley, D. M., (2018) Direct evidence of surface exposed water ice in the lunar polar regions, PNAS, Vol. 115, iss. 36, doi:10.1073/pnas.1802345115

Ligas, M. and Banasik, P., 2011. Conversion between Cartesian and geodetic coordinates on a rotational ellipsoid by solving a system of nonlinear equations (GEODESY AND CARTOGRAPHY), Vol. 60, No 2, 2011, pp. 145-159

Lucey, P. G., Petro, N, Hurley, D. M., Farrell, W. M., Prem, P., Costello, E. S., Cable, M. L., and others (2021), Volatile interactions with the lunar surface, Geochemistry, In Press, dio:10.1016/j.chemer.2021.125858

Marchi, S., Bottke, W. F., Cohen, B. A., Sunnenmann, K., Kring, D. A., McSween, H. Y., De Sanctis, M. S., and others, (2013), High-velocity collisions from the lunar cataclysm recorded in asteroidal meteorites, Nature Geoscience, Vol. 6, pp. 303-307, doi:10.1038/ngeo1769

Martinez, A., Siegler, M. A., (2021), A Global Thermal Conductivity Model for Lunar Regolith at Low Temperatures, Journal of Geophysical Research: Planets, Vol. 126, e2021JE006829, doi:10.1029/2021JE006829

McEwen, A. S., Bierhaus, E. B., The Importance of Secondary Cratering to Age Constraints on Planetary Surfaces, Annu. Rev. Earth Planet. Sci., Volume 34, 2006, Pages 535-567, doi: 10.1146/annurev.earth.34.125018

Melosh, H. J., Impact cratering : a geologic process, 1989, New York: Oxford University Press; Oxford : Clarendon Press

Melosh, H. J., Planetary surface processes. Cambridge University Press; 2011 Aug 25.

Minton, D. A., Richardson, J. E., Fassett, C. I., Re-examining the main asteroid belt as the primary source of ancient lunar craters, Icarus, Volume 247, 2015, Pages 172-190, ISSN 0019-1035, https://doi.org/10.1016/j.icarus.2014.10.018. (https://www.sciencedirect.com/science/article/pii/S0019103514005570)

Minton, D. A., Fassett, C. I., Hirabayashi, M., Howl, B. A., Richardson, J. E., The equilibrium size-frequency distribution of small craters reveals the effects of distal ejecta on lunar landscape morphology, Icarus,Volume 326,2019, Pages 63-87, ISSN 0019-1035, https://doi.org/10.1016/j.icarus.2019.02.021. (https://www.sciencedirect.com/science/article/pii/S0019103517308370)

Morbidelli, A., Nesvorny, D., Laurenz, V., Marchi, S., Rubie, D. C., Elkins-Tanton, L., Wieczorek, M., Jacobson, S., (2018), The timeline of the lunar bombardment: Revisited, Icarus, Vol. 305, pp. 262-276, doi:10.1016/j.icaurs.2017.12.046

Needham, D. H., Kring, D. A., (2017), Lunar volcanism produced a transient atmosphere around the ancient Moon, Earth and Planetary Science Letters, Vol. 478, 175-178, doi:10.1016/j.epsl.2017.09.002

Neukum G., Ivanov B.A., Hartmann W.K. (2001) Cratering Records in the Inner Solar System in Relation to the Lunar Reference System. In: Kallenbach R., Geiss J., Hartmann W.K. (eds) Chronology and Evolution of Mars. Space Sciences Series of ISSI, vol 12. Springer, Dordrecht. https://doi.org/10.1007/978-94-017-1035-0_3

Neukum, G.: 1983, *Meteoritenbombardement and Datierung Planetarer Oberflächen*, Habilitation Dissertation for Faculty Membership, Univ. of Munich, 186 pp.

Ong, L., Asphaug, E. I., Korycansky, D., Coker, R. F., (2010), Volatile retention from cometary impacts on the Moon, Icarus, Vol. 207, 578-589, doi:10.1016/j.icarus.2009.12.012

Öpik, E. J. (1960). The lunar surface as an impact counter. *Monthly Notices of the Royal Astronomical Society*, 120(5), 404–411. https://doi.org/10.1093/mnras/120.5.404

Paige, D. A., Siegler, M. A., Zhang, J. A., Hayne, P. O., Foote, E. J., Bennett, K. A., Vasavada, A. R., Greenhagan, B. T., Schofield, J. T., McCleese, D. J., and others. (2010), Diviner Lunar Radiometer Observations of Cold Traps in the Moon's South Polar Region, Science, Vol. 330, 6003, pp. 479-482, doi:10.1126/science.1187726

Pike, R. J. (1967), Schroeter's rule and the modification of lunar crater impact morphology, *J. Geophys. Res.*, 72(8), 2099– 2106, doi:10.1029/JZ072i008p02099.
Pike, R.J. (1974), Depth/diameter relations of fresh lunar craters: Revision from spacecraft data. Geophys. Res. Lett., 1: 291-294. https://doi.org/10.1029/GL001i007p00291

Pike, R. J., (1977), In: Lunar Planetary Science Conference Proceedings, Apparent depth/apparent diameter relation for lunar craters, Vol. 8, pp. 3427-3436

Pike R. J. 1980b. Formation of complex impact craters: Evidence from Mars and other planets. *Icarus* 43:1–19.

Pike, R. J. (1981), Target-Dependence of Crater Depth on the Moon. Lunar and Planetary Science Conference., pages 845-847, https://ui.adsabs.harvard.edu/abs/1981LPI....12..845P

Prem, P., Artemieva, N. A., Goldstein, D. B, Varghese, P. L., Trafton, L. M., (2015), Transport of water in a transient impact-generated lunar atmosphere, Icarus, Vol. 255, pp. 148-158, doi:10.1016/j.icarus.2014.10.2017

Prem. P., Goldstein, D. B, Varghese, P. L., Trafton, L. M., (2018), The influence of surface roughness on volatile transport on the Moon, Icarus, Vol. 299, pp. 31-45, doi:10.1016/j.icarus.2017.07.010

Prem, P., Goldstein, D. B., Varghese, P. L., Trafton, L. M., (2019), Coupled DSMC-Monte Carlo radiative transfer modeling of gas dynamics in a transient impact generated lunar atmosphere, Icarus, Vol. 326, pp. 88-104, doi:10.1016/j.icarus.2019.02.036

Richardson, J. E.,Cratering saturation and equilibrium: A new model looks at an old problem, Icarus, Volume 204, Issue 2,2009, Pages 697-715,ISSN 0019-1035, https://doi.org/10.1016/j.icarus.2009.07.029. (https://www.sciencedirect.com/science/article/pii/S0019103509003194)

Riedel, C., Minton, D. A., Michael, G., Orgel, C., van der Bogert, C. H., & Hiesinger, H. (2020). Degradation of small simple and large complex lunar craters: Not a simple scale dependence. Journal of Geophysical Research: Planets, 125, e2019JE006273. https://doi.org/10.1029/2019JE006273

Riris, H. *et al*., "The Lunar Orbiter Laser Altimeter (LOLA) on NASA's Lunar Reconnaissance Orbiter (LRO) mission," *2008 Conference on Lasers and Electro-Optics and 2008 Conference on Quantum Electronics and Laser Science*, 2008, pp. 1-2, doi: 10.1109/CLEO.2008.4551271.

Robbins, S.J., Watters, W.A., Chappelow, J.E., Bray, V.J., Daubar, I.J., Craddock, R.A., Beyer, R.A., Landis, M., Ostrach, L.R., Tornabene, L., Riggs, J.D. and Weaver, B.P. (2018), Measuring impact crater depth throughout the solar system. Meteorit Planet Sci, 53: 583-637. https://doi.org/10.1111/maps.12956

Rosenburg, M. A., Aharonson, O., Head, J. W., Kreslavsky, M. A., Mazarico, E., Neumann, G. A., Smith, D. E., Torrence, M. H., and Zuber, M. T. (2011), Global surface slopes and roughness of the Moon from the Lunar Orbiter Laser Altimeter, *J. Geophys. Res.*, 116, E02001, doi:10.1029/2010JE003716.

Ross, H. P. (1968). A simplified mathematical model for lunar crater erosion. *Journal of Geophysical Research*, 73, 1343–1354. https://doi.org/10.1029/JB073i004p01343

Senthil Kumar, P., V. Keerthi, A. Senthil Kumar, J. Mustard, B. Gopala Krishna, Amitabh, L. R. Ostrach, D. A. Kring, A. S. Kiran Kumar, and J. N. Goswami (2013), Gullies and landslides on the Moon: Evidence for dry-granular flows, J. Geophys. Res. Planets, 118, 206–223, doi:10.1002/jgre.20043.

Schorghofer, N., (2008), The Lifetime of Ice on Main Belt Asteroids, Icarus, Vol. 682, pp697, doi:10.1086/588633

Siegler, M. A., Paige, D., Williams, J. P., Bills, B., (2015) Evolution of lunar polar ice stability, Icarus, Vol. 255, 78-87, doi:10.1016/j.icarus.2014.09.037

Siegler, M. A., Miller, R. S., Keane, J. T., Laneuville, M., Paige, D. A., Matsuyama, I., Lawrence, D. J., Crotts, A., Poston, M. J., (2016), Lunar true polar wander inferred from polar hydrogen, Nature, Vol. 531, 7595, pp. 480-484, doi:10.1038/nature17166

Soderblom, L. A. (1970), A model for small-impact erosion applied to the lunar surface, *J. Geophys. Res.*, 75(4), 2655– 2661, doi:10.1029/JB075i014p02655.

Speyerer, E. J., Povilaitis, R. Z., Robinson, M. S., Thomas, P. C., & Wagner, R. V. (2016). Quantifying crater production and regolith overturn on the Moon with temporal imaging. *Nature*, 538(7624), 215–218. https://doi.org/10.1038/nature19829

Stopar, J. D., Robinson, M. S., Barnouin, O. S., McEwen, A. S., Speyerer, E. J., Henriksen, M. R., Sutton, S. S., (2017), Relative depths of simple craters and the nature of the lunar regolith, Icarus, Vol. 298, pp. 34-48, doi:10.1016/j.icarus.2017.05.022

Tye, A.R., Fassett, C.I., Head, J.W., Mazarico, E., Basilevsky, A.T., Neumann, G.A., Smith, D.E., Zuber, M.T., The age of lunar south circumpolar craters Haworth, Shoemaker, Faustini, and Shackleton: Implications for regional geology, surface processes, and volatile sequestration, Icarus, Volume 255, 2015, Pages 70-77, ISSN 0019-1035, https://doi.org/10.1016/j.icarus.2015.03.016. (https://www.sciencedirect.com/science/article/pii/S0019103515001165)

Wang, J., Kreslavsky, M. A., Liu, J., Head, J. W., Zhang, K., Kolenkina, M. M., & Zhang, L. (2020). Quantitative characterization of impact crater materials on the Moon: Changes in topographic roughness and thermophysical properties with age. Journal of Geophysical Research: Planets, 125, e2019JE006091. https://doi.org/10.1029/2019JE006091

Woronow, A. (1977). Crater saturation and equilibrium—A Monte Carlo simulation. *Journal of Geophysical Research*, 82, 2447–2456. https://doi.org/10.1029/JB082i017p02447

Xiao, Z., Mass Movements Related with Impact Craters, Reference Module in Earth Systems and Environmental Sciences, Elsevier, 2020, ISBN 9780124095489, https://doi.org/10.1016/B978-0-12-818234-5.00030-4. (https://www.sciencedirect.com/science/article/pii/B9780128182345000304)

Xie, M., Xiao, Z., & Xu, A. (2019). Time-dependent production functions of lunar simple craters on layered targets with consideration of topographic degradation. *Geophysical Research Letters*, 46, 10987– 10996. https://doi.org/10.1029/2019GL084097

Appendix

Table. A1. Data Compiled from this study

Name	Age [Ga] (Updated)	Age [Ga] (Ty2015 + De2020 + Ca2020)	Average slope angle [deg]	Diameter (km)	Crater depth [km]	Wall area [km2]	Erased volume [km3]	Resurfacing depth [km]
Amundsen	4	3.9	27.78	103.4	7.0783	5876	2993.08552	0.3564414216
Cabeus	4.15	3.88	18.25	100.6	4.6855	7763.9	13195.95614	1.6601794
Cabeus B	4.1	3.9	30.53	59.6	1.648	1912.46	2478.154028	0.8882718421
de Gerlache	4.15	3.9	26.5	32.7	5.299	730.55	1067.110069	1.270643828
Faustini	4.1	4.1	27.99	42.5	7.9475	1049.87	1097.531756	0.7736585927
Haworth	4.12	4.18	31.68	51.4	6.6957	1858.32	2486.566102	1.198350577
Nobile	4.18	3.8	20.59	79.3	1.19	3619.11	6165.423367	1.248322068
Scott	4.15	3.8	24.87	107.8	6.3044	6282.7	10182.44219	1.115641215
Shackleton	3.51	3.51	46.36	20.9	3.5331	310.797	5.328327341	0.01553132272
Shoemaker	4.2	4.15	20.82	51.8	6.2355	1747.36	2984.013845	1.41596146
Slater	3.8	3.8	17.3	25.1	3.1354	326.527	58.36701331	0.1179587458
Sverdrup	4	3.8	30	32.8	2.5284	583.98	328.6569561	0.3889602852
Unnamed 1	4	3.9	27.88	57.7	5.4489	1760.1	1063.401812	0.4066828781
Unnamed 2	4.15	3.7	37.93	26.8	2.058	479.65	732.0842254	1.297781502
Unnamed 3	3.4	3.4	30.56	22.3	4.1465	341.255	11.56404283	0.02960806899
Weichert J	3.6	3.2	32.14	34.9	7.1337	830.05	40.51150014	0.04234845691

All crater count data and slope values used for CSFDs and histogram plots are available here: https://docs.google.com/spreadsheets/d/1Ot9JWpDd3epV35UPqfOGCcUxv4teO99p/edit?usp=sharing&ouid=106336047333388681016&rtpof=true&sd=true